NACA

RESEARCH MEMORANDUM

CLASSIFICATION CHANGED TO __UNCLASSIFIED__
BY AUTHORITY OF NACA CLASSIFICATION CHANGE
NOTICE. CHANGE NO. _H.P.S. Ltr._ EFF. _Jan 20, 1971_
DH2/n/p

THE EFFECTS OF BODY VORTICES AND THE WING SHOCK-

EXPANSION FIELD ON THE PITCH-UP

CHARACTERISTICS OF SUPER-

SONIC AIRPLANES

By Jack N. Nielsen

Ames Aeronautical Laboratory
Moffett Field, Calif.

CLASSIFIED DOCUMENT

NATIONAL ADVISORY COMMITTEE
FOR AERONAUTICS
WASHINGTON
March 24, 1958

NATIONAL ADVISORY COMMITTEE FOR AERONAUTICS

RESEARCH MEMORANDUM

THE EFFECTS OF BODY VORTICES AND THE WING SHOCK-

EXPANSION FIELD ON THE PITCH-UP

CHARACTERISTICS OF SUPER-

SONIC AIRPLANES

By Jack N. Nielsen

SUMMARY

        A calculative technique is presented for predicting the influence
of body vortices and the wing shock-expansion field on the pitch-up
characteristics of supersonic airplanes to supplement calculative methods
for wing vortices which are well known. The method is applied to the
prediction of the pitch-up characteristics of four airplanes with high
tails, of which one serves as a calculative example. It was found that
the pitch-up characteristics as calculated are in good qualitative agree-
ment with the characteristics as measured in the wind tunnel. For the
four cases considered the wing influenced pitch-up through either the
shock-expansion field or the wing vortices. Shock-expansion interference
can be either stabilizing or destabilizing depending on the tail position
and Mach number. On the other hand body-vortex interference and wing-
vortex interference are destabilizing. For airplanes with relatively
small noses compared to the wing, the wing vortices dominate the pitch-
up tendency; and for airplanes with large noses relative to the wing, the
body vortices dominate. A pitch-up tendency dominated by body vortices
more readily results in actual pitch-up than one dominated by wing vor-
tices because body vortices increase in strength quadratically with angle
of attack, whereas wing vortices increase linearly. Areas of research
to improve the accuracy of the calculative method are outlined. It is
believed that the method in its present form is sufficiently accurate to
establish useful pitch-up boundaries.

INTRODUCTION

        Some supersonic airplanes encounter severe pitch-up tendencies,
particularly machines with the horizontal tail relatively high with

respect to the wing chord plane. It has been known for some time that wing vortices can induce pitch-up (refs. 1, 2, and 3). However, body vortices and the wing shock-expansion field can also induce such tendencies as discussed in reference 4. The possibility of calculating body-vortex effects rests on the availability of experimental data for the vortex strengths and positions (refs. 5, 6, and 7). The calculation of wing shock-expansion effects, on the other hand, is a direct application of shock-expansion theory (ref. 8). In reference 4 methods for calculating effects of body-vortex and shock-expansion fields are presented together with calculated examples to illustrate the main qualitative effects. This paper develops the subject of supersonic pitch-up in greater detail than is possible in a general unclassified paper such as reference 4. In particular, this paper includes a calculative example, and comparisons between calculated pitch-up characteristics and the characteristics measured in the wind tunnel for four airplanes over a Mach number range of 1.40 to 2.96.

SYMBOLS

a	radius of cylindrical portion of body
c_W	wing chord at wing-body juncture
C_L	lift coefficient
$(\Delta C_L)_T$	change in lift coefficient due to addition of tail
C_m	moment coefficient
$(\Delta C_m)_T$	change in moment coefficient due to addition of tail
$\left(\dfrac{dC_{L_T}}{d\alpha}\right)_M$	lift-curve slope per radian of tail alone at Mach number, M
d	body diameter
i_T	tail interference factor
L	lift
$L_{T(SE)}$	lift of tail alone in shock-expansion field of wing
$L_{T(\alpha)}$	lift developed by horizontal tail at body angle of attack, α
$L_{T(V)}$	lift on horizontal tail due to body vortices

l_T tail length, length from center of moments to center of lift of horizontal tail

l_r reference length

M free-stream Mach number

M_T Mach number at horizontal tail

q free-stream dynamic pressure

q_T dynamic pressure at horizontal tail

s_T tail semispan

S_R reference area

S_T tail area

r, θ polar coordinates in crossflow plane

Re Reynolds number

V free-stream velocity

v_θ, v_r tangential and radial components of vortex velocity, sketch (d)

x, y, z body axes, sketch (c)

y_i, z_i coordinates of image vortex in first quadrant, sketch (d)

y_o, z_o coordinates of external vortex in first quadrant, sketch (d)

x_S, y_S, z_S coordinates of vortex in first quadrant at separation

x_T coordinate of center of lift of tail

α angle of attack of body, radians or degrees

β $(M^2-1)^{1/2}$

β_T $(M_T{}^2-1)^{1/2}$

ϵ_T downwash angle at tail in wing shock-expansion field

Γ_B body-vortex strength, circulation about vortex

Γ_W wing-vortex strength

δ_T tail incidence

η_α angle-of-attack effectiveness of two-dimensional tail of
                 infinitesimal chord in shock-expansion field

$\bar{\eta}_\alpha$ average value of η_α over tail plan form

η_δ tail-incidence effectiveness of two-dimensional tail of
   infinitesimal chord in shock-expansion field

Subscripts

$T(V)$ acting on horizontal tail due to body vortices

B body

T horizontal tail

M evaluated at M

M_T evaluated at M_T

S body-vortex separation point

$T(SE)$ acting on horizontal tail in wing shock-expansion field with
                 no wing- or body-vortex interference

W wing

CAUSES OF PITCH-UP

        In their general sense "pitch-up" and "pitch-up tendency" involve
subjective pilot opinion of the dynamical condition of an airplane. In
this paper, however, the terms are used in more particular senses. By
pitch-up we mean a reversal in sign of C_{m_α} from negative to positive.
By a pitch-up tendency we mean an increase in the derivative $dC_m/d\alpha$ as
the angle of attack increases, and by nose-down tendency we mean a
decrease in $dC_m/d\alpha$ as the angle of attack increases. Pitch-up of air-
planes at supersonic speeds can result from a number of nonlinear effects.
One effect which has received widespread attention for missiles is the
interference of the wing vortices on the horizontal tail (refs. 1, 2,
and 3). Such interference is important in causing pitch-up for configura-
tions having wings and horizontal tails of nearly equal span. Airplanes
usually possess wings of greater span than the horizontal tail and thereby
reduce the possibility of pitch-up from this cause. In addition, mounting

the horizontal tail in a plane below that of the wing chord further reduces the tendency toward pitch-up due to wing vortices by increasing the distance of the tail from the vortices. However, for airplanes with high horizontal tails, wing vortices can cause significant pitch-up tendencies. For airplanes with high tails at least two other factors can also be of importance in longitudinal stability. The first of these factors is interference between body vortices and the horizontal tail as indicated in sketch (a) for a body-tail combination. For a range of
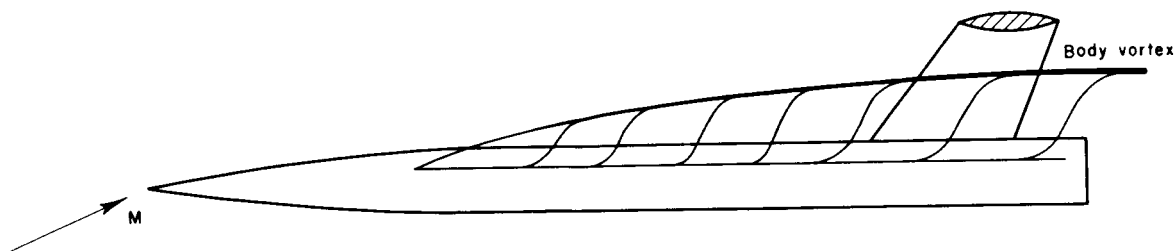
Sketch (a)

angles of attack, the vortices can pass close to the horizontal tail. In this position they can cause large changes in tail normal force if they are of appreciable strength. The addition of the wing can influence both the positions and strengths of the vortices at the tail for a fixed angle of attack. The effect of the vortices is to induce pitch-up by increasing the average downwash at the horizontal tail. It would be expected that such pitch-up, being a manifestation of viscosity, might be insensitive to Mach number and therefore might occur at subsonic as well as supersonic speeds.

The second important factor in the longitudinal stability of high-tail airplanes is the direct influence of the wing shock-expansion field on the horizontal tail as indicated in sketch (b). The shock-expansion field is two-dimensional corresponding to the wing chord at the wing-body juncture and neglecting three-dimensional effects of body interference. For the tail shown in sketch (b), the tail acts in a high
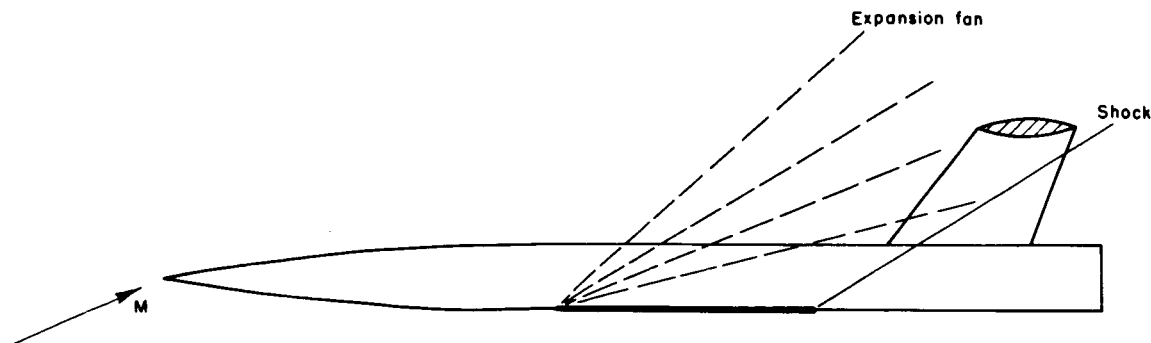
Sketch (b)

downwash field such that the local flow is nearly parallel to the tail chord. As the angle of attack of the airplane is increased, the tail moves downward relative to the trailing-edge shock wave out of the shock-expansion field and into a region of lower downwash. As a consequence, the tail download is decreased, resulting in a nose-down tendency. If the tail were initially above the expansion fan from the wing leading edge, it would move into the wave system of the wing with increasing angle of attack and cause a pitch-up tendency. Since the influence of the wing shock-expansion field on longitudinal stability depends on the location of the tail with respect to the field, it is sensitive to changes in Mach number. The wing shock-expansion field can cause both pitch-up and nose-down tendencies in contrast to body vortices which cause only pitch-up.

This paper presents methods for calculating the influence of body vortices and the wing shock-expansion field on pitch-up. Methods for calculating the effect of wing vortices on pitch-up are fully treated in reference 3. They are, therefore, not repeated here even though wing vortices assume importance for some of the airplanes to be considered. If the tail is in the wing shock-expansion field, it cannot "see" the wing trailing vortices. In this case we use the calculative method of this report for shock-expansion interference. If, however, the tail is behind the wing shock-expansion field and can "see" the wing trailing vortices, we use the calculative method of reference 3 for wing-vortex interference.

THEORY

In the theoretical sections which follow, we are concerned with calculating the lift and moment of the tail due to the body vortices and the same quantities for the tail embedded in the shock-expansion field of the wing. The total contributions of the tail can be written

$$\left.\begin{array}{l} (\Delta C_L)_T = (\Delta C_L)_{T(V)} + (\Delta C_L)_{T(SE)} \\[2ex] (\Delta C_m)_T = (\Delta C_m)_{T(V)} + (\Delta C_m)_{T(SE)} \end{array}\right\} \tag{1}$$

The section entitled "Theory of Body-Vortex Interference" gives explicit formulas for the quantities bearing the subscript $T(V)$, and the section entitled "Theory of Shock-Expansion Effects" gives explicit formulas for the quantities bearing the subscript $T(SE)$.

Theory of Body-Vortex Interference

The general method for calculating the change in longitudinal stability due to the body vortices is briefly the following: The body-vortex locations and strengths are obtained from experimental data correlations; the influence of the wing on their positions and strengths is calculated; and finally the tail load is estimated. These three steps will now be examined in detail.
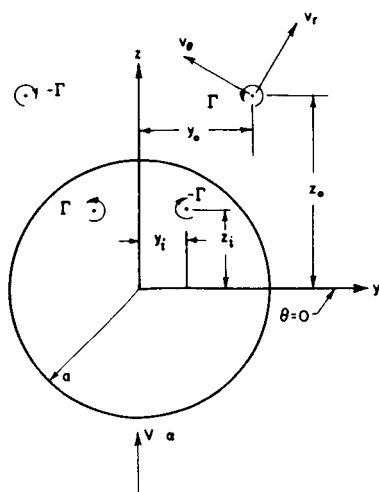
Vortex positions and strengths.- There exist several sets of data on the vortex positions and strengths for bodies of revolution at super-sonic speeds (refs. 5, 6, and 7). These data were obtained for the bodies of revolution and test conditions shown in figure 1 and can be correlated with fair success. A simplified model of the vortex separation is shown in sketch (c). At some distance x_S behind the apex of the body a pair

S, S': Vortex separation points
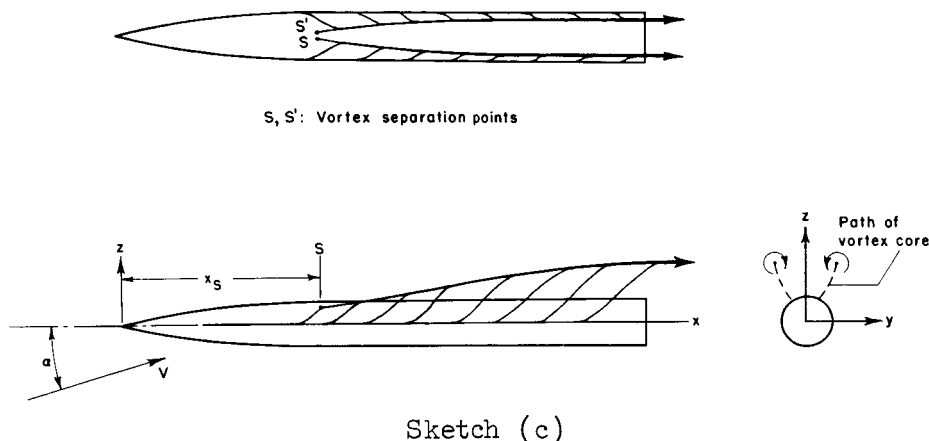
Sketch (c)

of vortices separates from the body. The pair increases in strength as it moves downstream as a result of small vortex filaments originating on the body and feeding into the cores. The dashed lines in the end view of the sketch are the paths of the vortex cores as they progress downstream.

The paths and vortex strengths of a particular body of revolution are dependent on the angle of attack α and the axial distance x behind the vertex of the body. If α and x could be replaced by a single nondimensional parameter, the prediction of vortex strengths and paths and the correlation of data on vortex strengths and paths would be simplified. The analysis of Appendix A based on the model of sketch (d) has resulted in such a parameter. It is shown in Appendix A that the vortex paths given by y_0/a and z_0/a and the nondimensional vortex strength $\Gamma_B/2\pi V a \alpha$ are functions only of $\alpha(x-x_S)/a$ for the vortex model considered in the analysis. Here x_S is the value of x for which the vortices separate from the body and is a function of α. The

experimental results of Jorgensen and Perkins, reference 5, for x_S are
shown in figure 2. The precise location of vortex separation could not
be determined but was found to lie within a
band about ±1 radius wide. The data for the
lateral and vertical vortex positions for all
three bodies are correlated in figure 3 as a
function of $\alpha(x-x_S)/a$. A curve has been
faired through each set of data to be used
for calculative purposes. A scatter about
the mean curves of ±0.1 includes most of the
data points and represents the approximate
accuracy of the wind-tunnel data. These
accuracies in vortex position are considered
satisfactory for qualitative stability cal-
culations since large changes in stability
do not usually occur for small changes in
vortex position.

Sketch (d)

The correlation of the nondimensional
vortex strength $\Gamma_B/2\pi Va\alpha$ from the three
tests is given in figure 4. It is observed that the data of Mello and
Raney are in good accord with one another over the range common to both.
The data of Jorgensen and Perkins lie somewhat higher than those of the
others, particularly at low values of $\alpha(x-x_S)/a$. This difference is
discussed in Appendix A. The correlation is inconclusive for small values
of $\alpha(x-x_S)/a$, but for larger values the percentage differences between
the three sets of data are small enough to be ignored for the purposes of
this report. For our examples severe pitch-up usually occurs for large
values of $\alpha(x-x_S)/a$.

Effect of wing on vortex paths and strengths.- A knowledge of the
vortex strengths and paths for a body of revolution provides only the
first step in the determination of the vortex strengths and positions
at the tail. It is necessary to take into account the influence of the
wing flow field on these quantities. A calculated vortex path including
wing effects is shown in figure 5 for zero wing thickness. In front of
the wing, body vortices develop as if the wings were not present, the
influence of the wing being felt as the vortices enter the expansion fan
from the leading edge. It is assumed that the body vortices follow the
streamlines of the wing shock-expansion field. The vortices are, there-
fore, deflected into a direction parallel to the free-stream direction
at the start of the expansion fan, and then are turned in traversing the
fan into a direction parallel to the wing chord. At the trailing-edge
shock wave the body vortices are again deflected in a direction parallel
to that of the free stream. It is difficult to assess the accuracy of
the assumption for nonslender wing panels. For one case a partial assess-
ment has been made. For the airplane model used in the calculative exam-
ple, it was found that the path of the body vortex seen in side view in

a schlieren picture for $\alpha = 16.7^\circ$ was in good accord with the calculated path. It is not clear that the lateral vortex positions were correctly predicted, however.

Although shock-expansion theory was used to compute the effect of the wing on the vortex paths for the examples of this paper, an alternate procedure is possible for slender configurations. For such configurations, calculation of the vortex paths with the wing panels present can be made by using slender-body theory and proceeding step by step. The practical calculation of the paths with any degree of precision is best accomplished by automatic computing methods. The appearance of vortices separating from the leading edges of the wing panels can further complicate the problem.

The addition of the wing to the body causes an alteration in the strength of the body vortices at the tail as well as a displacement in their positions. The gross effect of the wing is to prevent the forma-tion of feeding vortex filaments along the length of the body correspond-ing to the wing-body juncture. It is, therefore, <u>assumed</u> that the strengths of the vortices at the tail position correspond to those of the body alone, foreshortened by the chord at the wing-body juncture.

<u>Tail force due to body vortices.</u>- Several authors have made estimates of the forces on a tail due to vortices (refs. 1, 2, and 3). We will utilize the method based on the charts of tail interference factor in reference 3. The lift on the horizontal tail and body section due to a symmetrical pair of body vortices depends among other things on the posi-tion of the pair relative to the tail, the vortex strength, the tail lift-curve slope, and the tail-body configuration. It is possible to construct a convenient nondimensional factor to calculate the lift which depends only on the position of the vortex pair relative to the tail and the ratio of body radius to tail semispan. Such a factor, the quotient of a lift ratio and a nondimensional vortex strength, is the tail inter-ference factor, i_T, of reference 3, defined as follows:

$$i_T = \frac{L_T(v)/L_T(\alpha)}{(\Gamma_B/2\pi V a \alpha)(a/s_T)} \qquad (2)$$

Here $L_T(\alpha)$ is the lift on the tail alone, the two tail panels joined together at body angle of attack α evaluated at the local dynamic pressure and Mach number at the tail location. We will neglect any effect of body vortices on q or M at the tail but will include any effect of the shock-expansion field. We can put equation (2) into the more convenient form

$$(\Delta C_L)_{T(v)} = i_T \left(\frac{\Gamma_B}{2\pi V a \alpha}\right) \left(\frac{a}{s_T}\right) \left(\frac{s_T}{s_R}\right) \left(\frac{q_T}{q}\right) \alpha \left(\frac{dC_{L_T}}{d\alpha}\right)_{M_T} \qquad (3)$$

wherein $(dC_{L_T}/d\alpha)_{M_T}$ is based on the tail-alone area and local tail Mach number. The corresponding moment-coefficient increment due to the action of the body vortices on the tail is

$$(\Delta C_m)_{T(V)} = -\frac{l_T}{l_r}(\Delta C_L)_{T(V)} \tag{4}$$

The usefulness of equation (3) depends on the availability of charts for i_T, the tail interference factor. The charts of reference 3 for this quantity apply to the present case of two external vortices symmetrically disposed on each side of the body with midwing panels on each side. Similar charts can be constructed for one vortex and one panel. These charts would be required for determining forces on a single vertical tail in sideslip due to body vortices. Reverse-flow theorems have also been used to evaluate i_T (see ref. 3). One assumption underlying the application of the method of tail-force calculation based on i_T is that the vortices remain essentially parallel to the body axis during their passage past the tail; that is, the vortex paths in end view can be replaced by average positions. When the vortices are in close proximity to the tail surface, the lateral motions of the vortex in the crossflow plane can be large. Strong coupling then prevails between the vortex paths and the resulting tail force. Further theoretical and experimental study of this phenomenon is desirable.

Theory of Shock-Expansion Effects

In cases for which the shock-expansion effects of the wing on the tail are important, account can be taken of the changes in downwash angle, dynamic pressure, and Mach number at the tail by direct application of shock-expansion theory. The horizontal tail is usually of lesser span than the wing and lies behind the inboard sections of the wing. We, therefore, assume that the flow in the region of the tail is the two-dimensional shock-expansion field corresponding to the chord at the wing-body juncture. Any effects of wing-body interference or wing section in distorting the shock-expansion field are neglected.

The calculation of the lift of the tail in the shock-expansion field can conveniently be made in terms of two effectiveness parameters η_α and η_δ which will now be derived. Consider a horizontal tail in the shock-expansion field of the wing shown schematically in sketch (e). The angle of attack of the tail with respect to the local flow direction is $\alpha_W - \epsilon_T + \delta_T$. If q_T and M_T are the dynamic pressure and Mach number at the tail, the tail lift is

$$L_{T(SE)} = q_T(\alpha_W - \epsilon_T + \delta_T)\left(\frac{dC_{L_T}}{d\alpha}\right)_{M_T} S_T \tag{5}$$
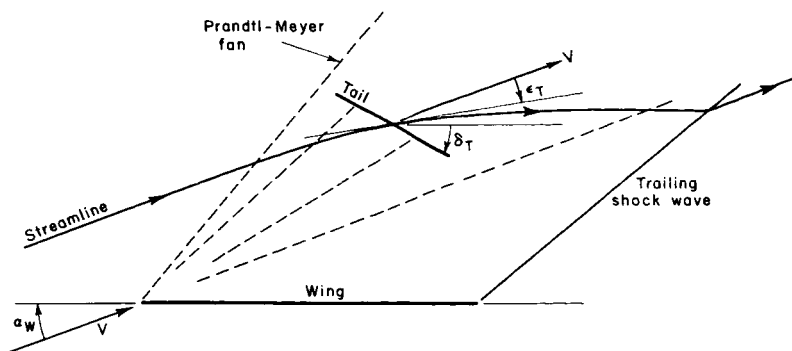
Sketch (e)

Let us make the tail lift in the shock-expansion field nondimensional by division with the lift of the tail in the free stream at α_W, which can be written as

$$L_T(\alpha_W) = q\alpha_W \left(\frac{dC_{L_T}}{d\alpha}\right)_M S_T \tag{6}$$

Performing the division yields

$$\frac{L_T(SE)}{L_T(\alpha_W)} = \left(\frac{q_T}{q}\right)\left(1 - \frac{\epsilon_T}{\alpha_W}\right)\frac{\left(\dfrac{dC_{L_T}}{d\alpha}\right)_{M_T}}{\left(\dfrac{dC_{L_T}}{d\alpha}\right)_M} + \frac{\delta_T}{\alpha_W}\left(\frac{q_T}{q}\right)\frac{\left(\dfrac{dC_{L_T}}{d\alpha}\right)_{M_T}}{\left(\dfrac{dC_{L_T}}{d\alpha}\right)_M} \tag{7}$$

Two effectiveness parameters are defined:

$$\eta_\alpha = \left(\frac{q_T}{q}\right)\left(1 - \frac{\epsilon_T}{\alpha_W}\right)\frac{\left(\dfrac{dC_{L_T}}{d\alpha}\right)_{M_T}}{\left(\dfrac{dC_{L_T}}{d\alpha}\right)_M} \tag{8}$$

$$\eta_\delta = \left(\frac{q_T}{q}\right)\frac{\left(\dfrac{dC_{L_T}}{d\alpha}\right)_{M_T}}{\left(\dfrac{dC_{L_T}}{d\alpha}\right)_M} \tag{9}$$

The lift on the tail in the shock-expansion field is now

$$L_{T(SE)} = L_T(\alpha_W) \left(\eta_\alpha + \frac{\delta_T}{\alpha_W} \eta_\delta \right) \tag{10}$$

With charts of η_α and η_δ, we can easily evaluate the lift of the tail in the shock-expansion field.

We will not be concerned with tail incidence and will not construct charts of η_δ. However, a series of charts have been prepared for η_α on the assumption that the tail lift-curve slope is inversely proportional to β as for a two-dimensional airfoil. Under these circumstances

$$\eta_\alpha = \left(\frac{q_T}{q} \right) \left(\frac{M^2-1}{M_T^2-1} \right)^{\frac{1}{2}} \left(1 - \frac{\epsilon_T}{\alpha_W} \right) \tag{11}$$

In the form of equation (11), η_α accounts for three effects of the wing shock-expansion field on the tail. The first factor accounts for change in dynamic pressure at the tail, the second factor accounts for change in tail lift-curve slope, and the third factor accounts for wing downwash at the tail. It is clear that for an infinitesimal tail, q_T, M_T, and ϵ_T are uniform over the tail so that η_α depends only on position in the shock-expansion field. Charts for η_α on this basis can be used for large tails by a suitable averaging technique. A series of charts of η_α have been prepared for angles of attack of 5°, 10°, 15°, and 20° and Mach numbers of 2, 3, 4, and 5. The general features of these charts given in figure 6 are of interest. In the upper expansion fan the effectiveness η_α falls continuously to zero as the tail moves downward or rearward. In the region of $\eta_\alpha = 0$ above the wing the flow is parallel to the wing. Behind the trailing-edge shock wave the flow is again essentially in the free-stream direction, and the value of η_α is high. The dashed lines represent surfaces of discontinuity across which tangential velocity differences exist but across which the flow direction and static pressure are continuous. For the higher angles of attack and Mach numbers, the dashed lines can vary a few degrees from the free-stream direction. It is noted that the effectiveness is usually greater below the dashed lines than above. This is not surprising in view of the greater shock losses through the upper trailing-edge shock than the lower leading-edge shock.

It might be surmised that a very low tail would have high effectiveness, η_α, for high supersonic speeds or hypersonic speeds because of the large increases in density known to exist on the impact side of the wing. Some increase in tail effectiveness above unity does occur for high angles of attack and large Mach numbers. When the effects of dynamic pressure, Mach number, and downwash are all taken into account, the percentage

increase in tail effectiveness is much less than the percentage increase in density. The effectiveness η_δ can, however, be very large at high α and high M.

The values of tail effectiveness for the finite tails of the examples to be considered were obtained by averaging the values from figure 6 over the horizontal-tail area. The values of lift and pitching moment contributed by the horizontal tail in the shock-expansion field are then

$$(\Delta C_L)_{T(SE)} = \bar{\eta}_\alpha \left(\frac{S_T}{S_R}\right) \alpha \left(\frac{dC_{L_T}}{d\alpha}\right)_M \tag{12}$$

$$(\Delta C_m)_{T(SE)} = -\left(\frac{l_T}{l_r}\right)(\Delta C_L)_{T(SE)} \tag{13}$$

The shock-expansion interferences on the tail lift and moment coefficients are $(1-\bar{\eta}_\alpha)$ times the tail contribution for $\eta_\alpha = 1$.

APPLICATION OF THEORY

The calculative procedures described have been applied to the prediction of the tail pitching moments of four airplanes with high tails, and the predicted pitching moments are compared with the experimental moments. The airplanes are shown in figure 7. For purposes of identification these models will be referred to, respectively, as the arrow-wing interceptor, research model, straight-wing airplane, and the swept-wing airplane. The data for the arrow-wing interceptor are hitherto unpublished data from the 1- by 3-foot supersonic wind tunnel. The data for the other airplanes as well as the dimensions were taken from references 9, 10, and 11. The arrow-wing interceptor serves as a model in the calculative example presented in Appendix B. An examination of the calculated pitch-up characteristics for the four airplanes and comparison between calculated and measured characteristics yields interesting results for the effect of configuration change on pitch-up.

Arrow-Wing Interceptor

Let us examine the calculated results for the arrow-wing interceptor. Specifically, let us consider the net result of the shock-expansion and body-vortex effects on the contribution of the tail to the pitching moment for $M = 1.97$. The variations with angle of attack of the significant parameters influencing the pitching moment are shown in figure 8, and the contributions to the tail pitching moment are shown in figure 9. First,

with regard to shock-expansion effects, figure 8(a) shows the tail
effectiveness η_α to be zero at $\alpha = 0^\circ$ increasing to nearly one at
$\alpha = 20^\circ$. This trend is the result of the tail being above the wing
trailing-edge shock wave at $\alpha = 0^\circ$ and beneath it at $\alpha = 20^\circ$. The
curve in figure 9(a) which includes only the shock-expansion losses thus
starts off tangent to the $\eta_\alpha = 0$ line, the horizontal axis, and curves
downward toward the $\eta_\alpha = 1$ line at high angles of attack. The shock-
expansion interference thus is stabilizing at the higher angles of attack
since it tends to decrease $dC_m/d\alpha$. Now with regard to body-vortex
effects, figure 8(b) shows the vertical approach of the body vortices
toward the plane of the tail as the angle of attack increases. As a
result, the tail interference factor shown in figure 8(c) increases with
angle of attack also. Figure 8(d) shows that the dependence of vortex
strength on angle of attack is quadratic since a constant value of
$\Gamma_B/2\pi Va\alpha$ indicates linear dependence. Since the contribution to the
pitching moment of the body vortices is proportional to the product of
the actual vortex strength times the tail interference factor, the con-
tribution increases very rapidly with α as shown in figure 9(a). It
is emphasized that vortex strength and tail interference factor are both
important in causing pitch-up in this case, and that in the pitch-up
region the shock-expansion interference is stabilizing. Some experimental
points are included in figure 9(a) for comparison with the theory. These
data, obtained in the 1- by 3-foot supersonic wind tunnel, confirm a def-
inite pitch-up. The agreement between experiment and theory is compatible
with the approximations of the theory.

A comparison of the calculated results shown in figure 9(b) for
$M = 2.96$ with those for $M = 1.97$ reveals significant Mach number effects.
In the first place the η_α variation with angle of attack shown in fig-
ure 8(a) reverses as the Mach number changes from 1.97 to 2.96. At the
lower Mach number the tail is in the shock-expansion field initially and
then moves beneath it, while at the high Mach number the tail is initially
above the field and moves down into it. For $M = 2.96$ the curve in fig-
ure 9(b) including shock-expansion losses starts off tangent to the
$\eta_\alpha = 1$ line and curves up toward the $\eta_\alpha = 0$ line. The shock-expansion
field is thus destabilizing at this Mach number in contrast to its stabi-
lizing influence at the lower Mach number. However, near $\alpha = 18^\circ$ the
tail starts to emerge from the shock-expansion field on the lower side,
and the tail effectiveness starts to rise as shown by figure 8(a). The
dotted lines in figures 8(a) and 9(b) correspond to the angle-of-attack
range for which this effect occurs. With regard to the effects of the
body vortices, figures 8(c) and 8(d) show small effect of Mach number on
the tail interference factor. The change in the contribution of the body
vortices with Mach number is thus dependent primarily on the change in
lift-curve slope of the horizontal tail and is destabilizing at both Mach
numbers. The net result of shock-expansion and body-vortex interferences
is that both are destabilizing at $M = 2.96$, leading to the probability
of pitch-up at lower angles of attack than at $M = 1.97$.

Research Model

The variations with angle of attack of the significant parameters influencing the pitching moment due to the tail for the research model are shown in figure 10, and the contributions of the tail to the pitching moment are given in figure 11. Shock-expansion theory shows that the leading-edge shock wave detaches near $\alpha = 10^\circ$. At this condition the tail is already well out of the shock-expansion field. Thus the interference of the wing vortices rather than the shock-expansion field is important in the upper angle-of-attack range where pitch-up might occur. Accordingly, we use the wing-vortex interference method of reference 3 in calculating the effect of the wing on the tail.

In figure 10(b) the vortex heights at the tail are shown for the wing and body vortices. The body vortices move across the tail at about 19° angle of attack. The curve of tail interference factor for the body vortices in figure 10(c) shows a maximum near $\alpha = 19^\circ$ where it crosses the tail. The tail interference factor is less for the body vortices than the wing vortices, even though the body vortices cross the tail whereas the wing vortices do not. The body vortices are usually located inboard of the tail tip in relative proximity to the body in contrast to the wing vortices which are usually outboard of the tail tip. In the inboard position the body vortices are closer to their images inside the body than are the wing vortices to their images. If the body vortices actually closely approach the body, their images effectively cancel their effect on the tail. As a result the values of i_T for body vortices are characteristically less than those for wing vortices. The nondimensional vortex strength of the wing vortices shown in figure 10(d) is more than twice that of the body vortices. The reason for the difference is that the body section in front of the wing has small plan-form area in comparison to the wing. These facts explain the larger influence of the wing vortices than of the body vortices shown in figure 11. One point should be mentioned in connection with the body vortices. At $\alpha = 19^\circ$ where the tail interference factor peaks in figure 10(c) the body vortices are in close proximity to the tail - so close that they come into contact with the boundary layer. Also there is a rapid lateral movement of the vortices because of their mirror images. The influences of the lateral motion and of the boundary layer are neglected in calculating the tail interference factor. Therefore, the peak in the pitching moment due to a peak in i_T has been rounded off, particularly since no peak is found experimentally.

In figure 11, data from reference 9 (supplemented by additional measurements at the larger angles of attack) are shown for comparison with the prediction. The theory indicates a pitch-up at the high angles of attack with a reversal of the slope of the pitching-moment curve. The experiment indicates a pitch-up tendency with zero slope at $\alpha = 20^\circ$. The calculated pitch-up curve is dominated by the wing vortices up to an

angle of attack of 20°. Since neither the tail interference factor nor the nondimensional vortex strength for the wing vortices changes much with α, a strong calculated pitch-up is not predicted as it would be if the body vortices were dominant.

Straight-Wing Airplane

The relative proportions of the forebody and wing areas for the straight-wing airplane differ significantly from those of the previous model. In the present example the plan-form area of the fuselage ahead of the wing is about equal to the wing area, whereas in the previous example the forebody area was only about one-fifth of the wing area. This condition tends to increase the importance of body-vortex effects. Also, the Mach number for the present example of 2.01 is larger than the value of 1.4 for the previous example. As a result, the horizontal tail of the straight-wing airplane is in the wing shock-expansion field, and we must treat the wing-tail interference by shock-expansion methods and ignore the wing-vortex interference. Since data are given in reference 10 for the tail contribution to C_m with wing off and wing on, we will investigate the effect of the wing on pitch-up.

The variations with α of the significant parameters influencing the pitching moment due to the tail are presented in figure 12, and the contributions of the tail to the pitching moment are presented in figure 13. The low values of η_α in figure 12(a) show the importance of shock-expansion interference. The body-vortex heights at the tail are shown for the wing-on and wing-off conditions in figure 12(b). With the wing on, the vortices are closer to the horizontal tail because of the deflection of the vortices by the wing trailing-edge shock wave. The tail interference factors with the wing on and the wing off are not greatly different. The nondimensional vortex strength for the wing-off case is greater than for the wing-on case because the wing inhibits crossflow around the body at the root chord.

The calculated contributions of the tail to the pitching moment for both conditions are compared in figure 13. The wing-on case shows a stabilizing effect of shock-expansion interference at high angles of attack. However, the destabilizing influence of the body vortices induces a pitch-up at the higher angles of attack. The wing-off case exhibits a stronger calculated pitch-up than the wing-on case because the viscous crossflow is not blanketed by the wing. Data from reference 10 are included in figure 13 for comparison with the theory. Agreement for the body-tail combinations is somewhat better than for the wing-body-tail combination. However, in view of the approximation in the calculative method, the over-all agreement is considered satisfactory.

Swept-Wing Airplane

The variations with α of the significant parameters influencing the
pitching moment due to the tail for the present swept-wing airplane are
presented in figure 14, and the contributions of the tail to the pitching
moment are presented in figure 15. The position of the tail for this model
is such that wing-tail interference results from the wing vortices and not
the shock-expansion field. We, therefore, consider the combined influence
of body vortices and wing vortices on the pitching moment. The heights of
the vortices at the tail shown in figure 14(a) show the body vortices
intersecting the horizontal tail near $\alpha = 18^{\circ}$. The tail interference
factor for the body vortices exhibits the characteristic peaks near this
angle of attack. The tail interference factor and vortex strength are
generally less for the body vortices than the wing vortices.

The contributions of the tail to the pitching moments shown in
figure 15 consist of a pitching-moment increment due to tail incidence,
one due to wing-tail interference, and a lesser one due to body-vortex
interference. Even though the body vortices have effects of lesser mag-
nitude than the wing vortices, their influence on pitch-up is nevertheless
greater because of the rate of change of their influence with angle of
attack. The experimental points taken from reference 11 and included in
figure 15 for comparison with theory include any influence of jet flow on
the pitching moment during the wind-tunnel test. The good agreement
between experiment and theory is interpreted to mean that the interference
of the jet flow on the high horizontal tail is not large.

CONCLUDING REMARKS

The study of the four airplanes reveals certain generalizations
concerning the pitch-up of high-tail airplanes at supersonic speeds. The
influence of the wing is manifest either through the shock-expansion
field or through wing vortices. In the former case the influence can be
either stabilizing or destabilizing, depending on the Mach number, while
in the latter case the influence is destabilizing. The influence of the
body nose is manifest through body vortices acting on the horizontal-tail
plane and is always destabilizing. In contrast to the wing vortices or
shock-expansion field which cause moment variations moderately nonlinear
in angle of attack, the body vortices produce sharper nonlinearity which
can lead to sudden pitch-up. The effect of the body vortices can be
diminished (1) by decreasing the length of the fuselage in front of the
wing, (2) by reducing the radius of the fuselage, (3) by positioning the
tail to reduce the tail interference factor, and (4) by changing the tail
taper ratio to reduce the tail interference factor for vortices well
inboard of the tail tips. How these changes affect pitch-up can be esti-
mated by the calculative method illustrated herein. Therefore, the

calculative method can be used to establish approximate pitch-up boundaries.
No claim is made to great quantitative accuracy for the calculative method,
but it is believed that it is sufficiently accurate for most qualitative
purposes. Improvement of the accuracy of the method hinges on (1) better
information for vortex strengths and paths for more body shapes over wider
ranges of Reynolds numbers and Mach numbers, (2) better understanding of
the influence of the wing on the vortex paths, (3) better methods of
evaluating the influence of vortices on lifting surfaces, particularly in
their immediate proximity, and (4) better methods for evaluating the
downwash behind wing-body combinations at high angles of attack.

Ames Aeronautical Laboratory
    National Advisory Committee for Aeronautics
        Moffett Field, Calif., Dec. 23, 1957

APPENDIX A

THEORY OF VORTEX PATHS AND STRENGTHS FOR FLOW

OVER AN INCLINED BODY OF REVOLUTION

In this appendix the equations of vortex motion and vortex strength are derived to indicate the basis for correlating the experimental values of the vortex positions and strengths. The second purpose is to discuss the theoretical solutions and the experimental correlations for the vortex positions and strengths together with the prospects for improved solutions. The theoretical treatment is based on the crossflow model of sketch (d). It is assumed that the steady vortex flow past the body of revolution is equivalent to the unsteady flow of two external vortices with time-dependent strengths in the presence of a circular cylinder in uniform flow. Although there is some indication on the basis of the work of Mello (ref. 6), that up to 30 percent of the total vorticity can lie in the sheets feeding the vortex cores, we nevertheless assume that all vorticity is concentrated in the cores. The refinement possible by consideration of separate feeding sheets involves mathematical complications beyond the scope of this report.

Since the steady three-dimensional vortex flow is related to an unsteady two-dimensional flow, the axial distance x is now related to the time directly

$$x = Vt \qquad (A1)$$

The velocity components v_r and v_θ of the right external vortex are due to potential crossflow and the other three vortices as follows:

	Radial velocity	Tangential velocity
Potential crossflow:	$\alpha V \sin\theta(1 - a^2/r^2)$	$\alpha V \cos\theta(1 + a^2/r^2)$
Left external vortex:	$-(\Gamma/4\pi r)\tan\theta$	$-(\Gamma/4\pi r)$
Right image vortex:	0	$-(\Gamma/2\pi r)(1 - a^2/r^2)$
Left image vortex:	$\dfrac{\Gamma}{2\pi}\dfrac{a^2 r \sin 2\theta}{r^4 + 2a^2 r^2 \cos 2\theta + a^4}$	$\dfrac{\Gamma}{2\pi}\dfrac{r(r^2 + a^2 \cos 2\theta)}{r^4 + 2a^2 r^2 \cos 2\theta + a^4}$

Let us now consider the nondimensional variables to be used in the equations of vortex motion

Vortex strength: $\qquad \Gamma/2\pi V\alpha a = \Gamma^*$

Axial distance: $\qquad \alpha(x - x_S)/a = x^*$

Radial distance: $\qquad r/a = r^*$

In terms of these parameters, the equations of motion become

$$\frac{dr^*}{dx^*} = \sin\theta\left(1 - \frac{1}{r^{*2}}\right) - \frac{\Gamma^*}{r^*}\tan\theta + \frac{\Gamma^* r^* \sin 2\theta}{r^{*4} + 2r^{*2}\cos 2\theta + 1} \qquad (A2)$$

$$r^*\frac{d\theta}{dx^*} = \cos\theta\left(1 + \frac{1}{r^{*2}}\right) - \frac{\Gamma^*}{r^*} + \frac{\Gamma^* r^*(r^{*2} + \cos 2\theta)}{r^{*4} + 2r^{*2}\cos 2\theta + 1} - \frac{\Gamma^*}{r^* - \dfrac{1}{r^*}} \qquad (A3)$$

If for x^* equal to zero the initial values of Γ_S^*, r_S^*, and θ_S for vortex separation are known, the vortex paths can be obtained by step-by-step integration of equations (A2) and (A3). However, to carry out the integration the dependence of Γ^* on x^* must be known.

A relationship between Γ^* and x^* can be established if the variation with x^* of the crossflow drag coefficient, c_{d_c}, is known. The definition of c_{d_c} is given by the following equation for the normal force on the body due to viscous crossflow between positions x and x_S.

$$N = c_{d_c}q(2a)(x - x_S)\alpha^2 \qquad (A4)$$

As defined, c_{d_c} is the average crossflow drag coefficient between x and x_S. Let us now assume that the entire viscous cross force normal to the body axis is represented by horseshoe vortices of which the external vortices and the image vortices of sketch (d) are the trailing members. By the usual relationship of lifting-line theory the lift of a horseshoe vortex is $\rho V\Gamma$ per unit span so that

$$N = 2\rho V\Gamma(r - a^2/r)\cos\theta \qquad (A5)$$

From equations (A4) and (A5) we obtain the desired relationship

$$\Gamma^* = \left(\frac{c_{d_c}}{4\pi}\right)\frac{x^*}{(r^* - 1/r^*)\cos\theta} \qquad (A6)$$

The vortex paths can now be obtained by substituting equation (A6) for Γ^* into equations (A2) and (A3). We then have two simultaneous differential equations for r^* and θ which can be integrated step-by-step to obtain the path. If the integration is started at the vortex separation point, the paths will depend on r_s^*, θ_s, and c_{d_c}, so that the solution for the vortex paths and strengths has the form

$$\left.\begin{array}{l} r^* = r^*(r_s^*,\theta_s,c_{d_c},x^*) \\[2ex] \theta = \theta(r_s^*,\theta_s,c_{d_c},x^*) \\[2ex] \Gamma^* = \Gamma^*(r_s^*,\theta_s,c_{d_c},x^*) \end{array}\right\} \qquad (A7)$$

To correlate the vortex positions and strengths we might plot Γ^*, r^*, and θ against x^*. For small values of x^* it would be expected that the paths and strengths would depend significantly on the initial value of the vortex separation position, r_s^* and θ_s. However, for larger values of x^* it might be anticipated that the paths and strengths would no longer be sensitive to the initial conditions. Instead of determining a relationship between Γ^* and x^* by specifying the variation of c_{d_c} with α, we could have tried the alternate scheme of specifying the variation of the stagnation point θ_s with x^*. This alternate scheme would not change the form of the correlation.

The correlation of the vortex positions shown in figure 3 is only slightly less accurate than the measurements of vortex position could be repeated. The correlation of the nondimensional vortex strengths shown in figure 4 is not accurate at low values of $\alpha(x-x_S)/a$. It is desirable to know how the correlation was obtained to interpret this discrepancy. The values of x_S in the parameter $\alpha(x-x_S)/a$ in all three cases were taken from figure 2 which represents results of reference 5. The values of x_S measured in reference 6 are in good accord with those of reference 5, but no values of x_S are given in reference 7. In each investigation a different method was used to obtain the total vortex strength. Mello measured the individual strengths of both the feeding sheet and the concentrated core by measuring velocities tangential to a contour enclosing the vorticity and then calculating the circulation of the contour. Raney determined his vortex strengths by computing the theoretical flow velocities on the basis of the vortex model of sketch (d) and adjusting the vortex strengths so that the calculated velocities agree with the measured ones. Jorgensen and Perkins obtained the vortex strength by three methods. The one used in the present correlation is that calculated from equation (A5) using measured vortex positions and body normal-force distributions. The lift associated with the vortex is taken as the normal force as measured minus the "potential lift" calculated by the theory of Tsien, reference 12. An examination of the data of Jorgensen and Perkins shows that lift associated with the vortex exists in front of the vortex separation point. Such a fact must mean that the vortex strength is greater than zero before separation and must thereby account for the

finite values of vortex strength when $\alpha(x-x_S)/a$ is zero. Measurements in the neighborhood of vortex separation that will resolve this question have not yet been made.

In accordance with the second purpose of this appendix, solutions of equations (A2) and (A3) for the path were obtained by numerical integration on a computing machine for various values of c_{d_c}, $r_S{}^*$, and θ_S. It was immediately apparent that the path is extremely sensitive to the assumed vortex separation position. The study resolved itself into finding a vortex separation point and crossflow drag coefficient which would give vortex paths in the crossflow plane in approximate agreement with the mean path from the correlation. Such a path based on $c_{d_c} = 1.2$, $r_S{}^* = 1.062$, and $\theta_S = 50°$ is shown in figure 16 and compared with the mean experimental path. The agreement is only fair. The initial fluctuation in the calculated path is not significant, but the reversal of the vortex path from upward to downward is of interest. The reversal point is reached when the external vortices become so strong that their mutual downward-induced velocities approximately equal the free-stream velocity. The looping of the vortex path after reversal may not be physically significant since the main core may break away from the feeding sheet, which then starts a new core.

It is apparent that the present theory is inadequate for replacing the experimental correlations of the vortex positions and strength. In view of the desirability of putting the vortex theory on a sound theoretical basis, several suggestions for improving the theory are advanced. The theoretical model in the first place is incorrect in its neglect of the vortex feeding sheet. Some account of the feeding sheet on the path of the vortex core can be taken by including, in the equations of motion, the Edwards' term (refs. 13 and 14) designed to keep the net forces on the combination of the feeding sheet and core zero.

Another weakness of the present solution is that it does not take into account the variation of the crossflow drag coefficient with x^* known experimentally to exist. If the alternate boundary condition of specifying the leeward stagnation point had been used, the variation of the stagnation point with x^* shown by the data of Jorgensen and Perkins would also have to be taken into account, particularly near vortex separation. However, it is felt that either of these two alternate boundary conditions is capable of improvement. The feeding sheets are streamlines of the crossflow originating behind the separation points on the sides of the body. The effect of the feeding sheets is to streamline the body and reduce the velocities at the side edges of the body. The longer the vortex sheet, the lower the velocities at the side edges. A relationship between the vortex position and strength can thus be obtained by considering the change in side-edge velocity due to the streamlining effect of the vortex sheet. It is felt that a boundary condition of this type, based on a streamline model, is closer to the physical features of the real flow than a specification of the crossflow drag coefficient or the

leeward stagnation point based on the present model. It should, therefore, lead to greater accuracy than the present solution. Whether such an improvement coupled with the use of the Edwards' term will give adequate solutions for small x^* is questionable. Accurate solutions for small values of x^* almost certainly will be dependent on the Reynolds number since the positions of vortex separation which strongly influence such solutions are controlled by the boundary layer.

APPENDIX B

CALCULATIVE EXAMPLE

As a calculative example consider the airplane with a high tail shown in figure 7(a). We will calculate the effect of the body vortices and the shock-expansion field on the pitching moment due to the tail.

If the influence of the body vortices is considered, the first quantity in equation (3), i_T, depends on the vortex locations at the longitudinal position of the centroid of the horizontal tail. The calculated paths are shown in side view for $\alpha = 20^\circ$, $M = 1.97$, in figure 5. The initial value of x_S at the separation point of the body vortices obtained from figure 2 for $\alpha_B = 20^\circ$ is

$$\frac{x_S}{a} = 7$$

The values of y_S/a and z_S/a are obtained from figures 3(a) and 3(b) for zero values of $\alpha(x-x_S)/a$.

$$y_S/a = 0.50 \qquad z_S/a = 0.85$$

The correlation curves of figure 3 are used to obtain the vortex paths up to the leading edge of the expansion fan. On selected Mach waves in the expansion fan the local flow directions are indicated, and the body-vortex paths are drawn to conform with the streamlines. At the trailing-edge shock the vortices are assumed to be deflected in the streamwise direction. The vertical position of the vortices at the tail is now

$$\left(\frac{z_o}{a}\right)_T = 4.35$$

The lateral vortex position is assumed to be unchanged from its value where it enters the shock-expansion field:

$$\left(\frac{y_o}{a}\right)_T = 0.70$$

The value of i_T taken from reference 3 is found to be

$$i_T = -1.65$$

since the vortices have the same effect for the same distance above or below the tail.

The second parameter in equation (3), the nondimensional vortex strength, is obtained from figure 4. For the present model

$$\frac{x_S}{a} = 7, \quad c_W = 3.55, \quad a = 0.575, \quad x_T = 16.16$$

The parameter $\alpha(x-x_S)/a$ corresponding to a body foreshortened by the wing chord at the juncture is

$$\alpha\left(\frac{x}{a} - \frac{x_S}{a}\right) = \frac{20}{57.3}\left(\frac{16.16 - 3.55}{0.575} - 7\right) = 5.25$$

From figure 4 the corresponding vortex strength is

$$\frac{\Gamma_B}{2\pi V a \alpha} = 1.5$$

The remaining quantities in equation (3) are

$$a = 0.575$$

$$s_T = 1.25$$

$$S_T = 1.80$$

$$S_R = 14.37$$

$$\frac{q_T}{q} = 0.877, \text{ shock-expansion theory}$$

$$M_T = 1.85, \text{ shock-expansion theory}$$

$$\left(\frac{dC_{L_T}}{d\alpha}\right)_{M_T} = \frac{4}{\beta_T} = 2.57, \text{ supersonic wing theory}$$

$$l_T = 6.92$$

$$l_r = 2.85$$

The length l_T is taken as the distance between the center of moments, 9.24 inches behind the body vertex, and the 2/3-root-chord position of the tail. The contribution of the tail to the moment coefficient because of vortices is thus

$$(\Delta C_m)_{T(V)} = -(-1.65)(1.5)\left(\frac{0.575}{1.25}\right)\left(\frac{1.80}{14.37}\right)\left(\frac{6.92}{2.85}\right)(0.877)\left(\frac{20}{57.3}\right)(2.57)$$

$$= 0.27$$

With regard to the effects of the shock-expansion field, the tail effectiveness η_α is shown in figure 8(a) as obtained from figure 6. We have from equations (12) and (13)

$$(\Delta C_m)_T = -\left(\frac{6.92}{2.85}\right)\left(\frac{1.80}{14.37}\right)\left(\frac{20}{57.3}\right)(2.36)\eta_\alpha$$

$$= -0.25\eta_\alpha$$

REFERENCES

1. Edwards, S. Sherman: Experimental and Theoretical Study of Factors Influencing the Longitudinal Stability of an Air-to-Air Missile at a Mach Number of 1.4. NACA RM A51J19, 1952.

2. Edelman, G. M.: Wing-Body and Wing-Body-Tail Interaction at Supersonic Speeds for Generalized Missile Configurations at High Angles of Attack. U. S. Navy Symposium on Aeroballistics, Pasadena, Calif., May 13-14, 1952.

3. Pitts, William C., Nielsen, Jack N., and Kaattari, George E.: Lift and Center of Pressure of Wing-Body-Tail Combinations at Subsonic, Transonic, and Supersonic Speeds. NACA Rep. 1307, 1957.

4. Nielsen, Jack N., and Kaattari, George E.: The Effects of Vortex and Shock-Expansion Fields on Pitch and Yaw Instabilities of Supersonic Airplanes. IAS Preprint No. 743, 1957.

5. Jorgensen, Leland H., and Perkins, Edward W.: Investigation of Some Wake Vortex Characteristics of an Inclined Ogive-Cylinder Body at Mach Number 1.98. NACA RM A55E31, 1955.

6. Mello, John F.: Investigation of Normal-Force Distributions and Wake Vortex Characteristics of Bodies of Revolution at Supersonic Speeds. APL/JHU Rep. CM 867, Johns Hopkins Univ., April 1956.

7. Raney, D. J.: Measurement of the Cross Flow Around an Inclined Body at a Mach Number of 1.91. R.A.E. TN Aero. 2357, Jan. 1955.

8. Ames Research Staff: Equations, Tables, and Charts for Compressible Flow. NACA Rep. 1135, 1953.

9. Stivers, Louis S., Jr., and Lippmann, Garth W.: Effects of Vertical Location of Wing and Horizontal Tail on the Aerodynamic Characteristics in Pitch at Mach Numbers from 0.60 to 1.40 of an Airplane Configuration With an Unswept Wing. NACA RM A57I10, 1957.

10. Spearman, M. Leroy, and Driver, Cornelius: Longitudinal and Lateral Stability Characteristics of a Low-Aspect-Ratio Unswept-Wing Airplane Model at Mach Numbers of 1.82 and 2.01. NACA RM L56H06, 1957.

11. Carmel, Melvin M., and Turner, Kenneth L.: Investigation of Drag and Static Longitudinal and Lateral Stability Characteristics of a Model of a 40.4° Swept-Wing Airplane at Mach Numbers of 1.56 and 2.06. NACA RM L56I17a, 1957.

12. Tsien, Hsue-Shen: Supersonic Flow Over an Inclined Body of Revolu-
     tion. Jour. Aero. Sci., vol. 5, no. 12, Oct. 1938, pp. 480-483.

13. Cheng, Hsien K.: Remarks on Nonlinear Lift and Vortex Separation.
     Jour. Aero. Sci., vol. 21, no. 3, Readers' Forum, March 1954,
     pp. 212-214.

14. Edwards, R. H.: Leading-Edge Separation From Delta Wings. Jour.
     Aero. Sci., vol. 21, no. 2, Readers' Forum, Feb. 1954, pp. 134-135.
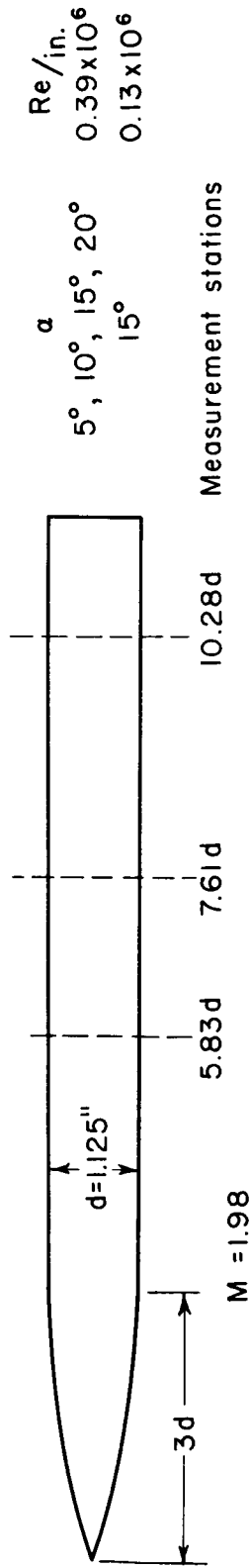
(a) Ogive-cylinder of reference 5.
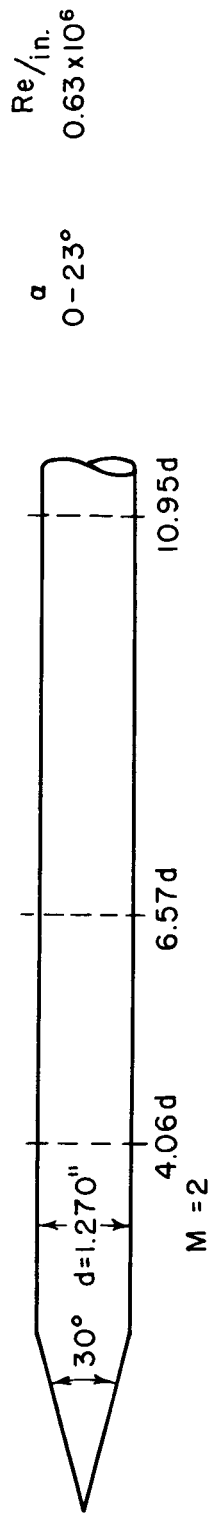
(b) Cone-cylinder of reference 6.
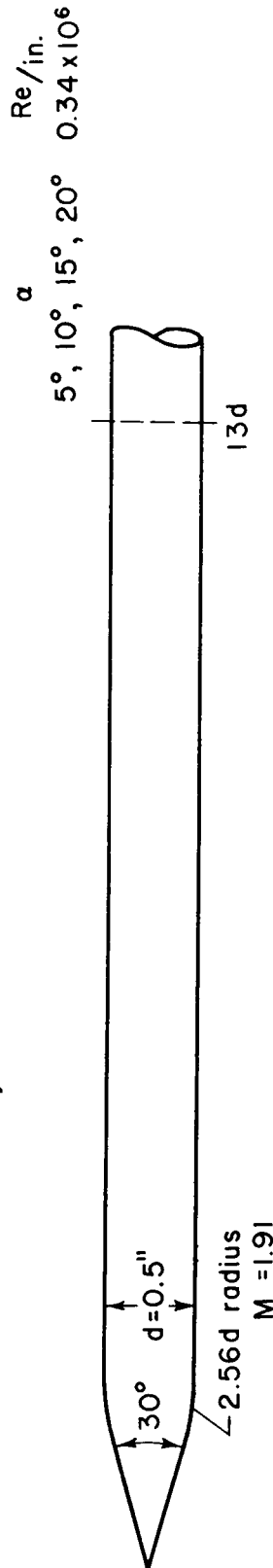
(c) Modified cone-cylinder of reference 7.

Figure 1.- Bodies of revolution and range of variables for correlation of body vortex strengths and positions.
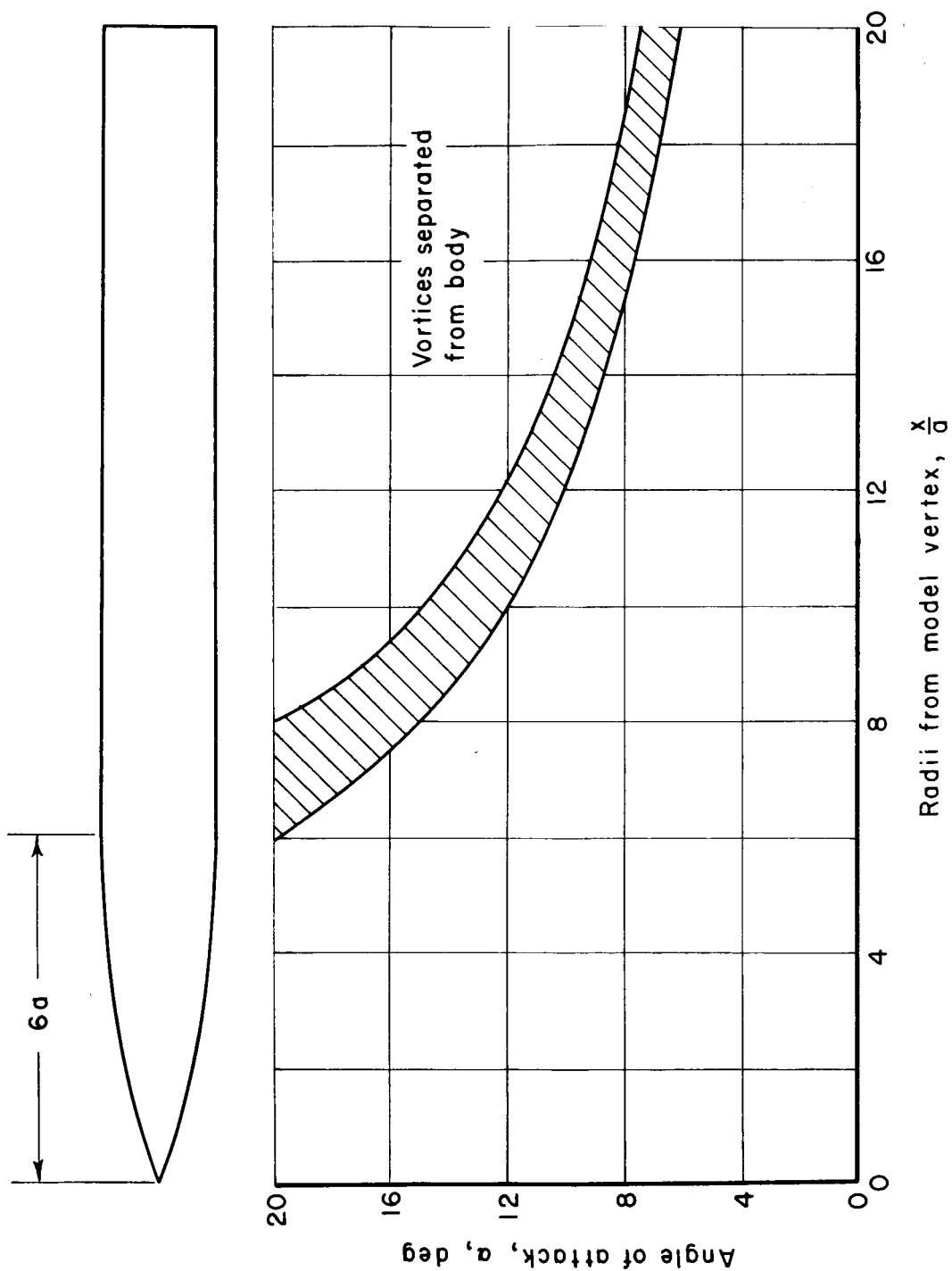
Figure 2.- Approximate axial location of vortex separation for ogive-cylinder of reference 5; M = 1.98.
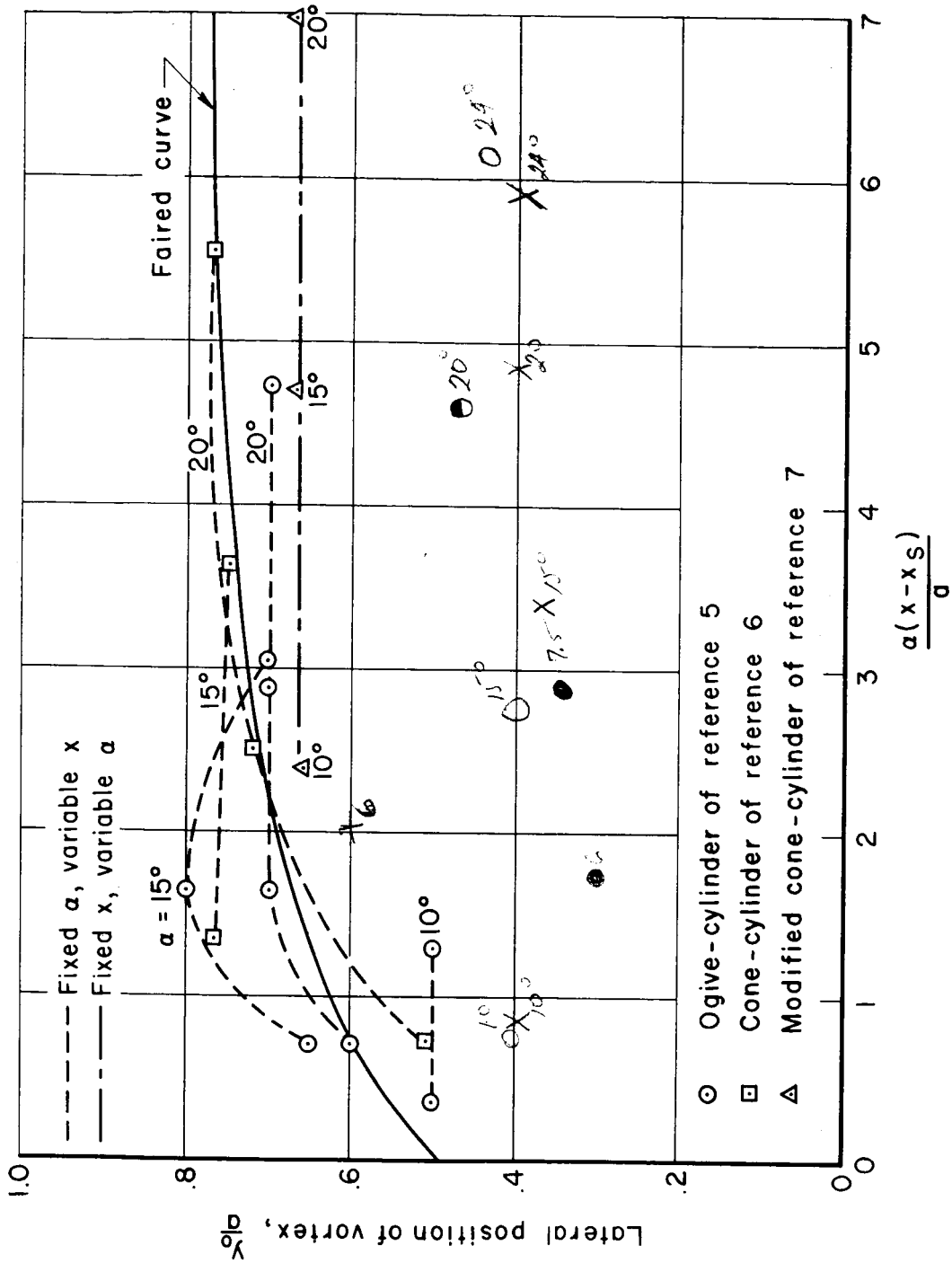
(a) Lateral position.

Figure 3.- Correlation of vortex positions for three bodies of revolution.
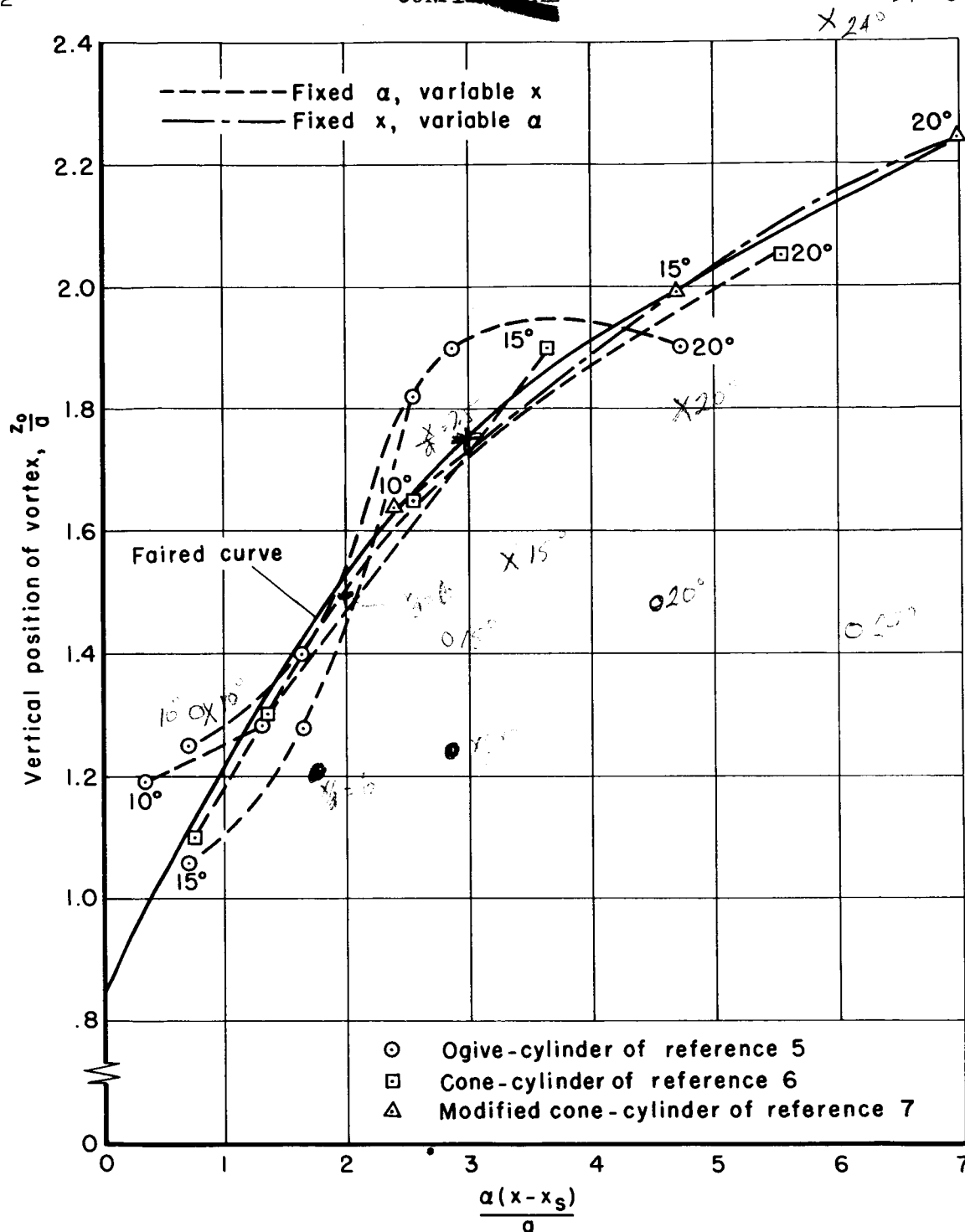
(b) Vertical position.

Figure 3.- Concluded.
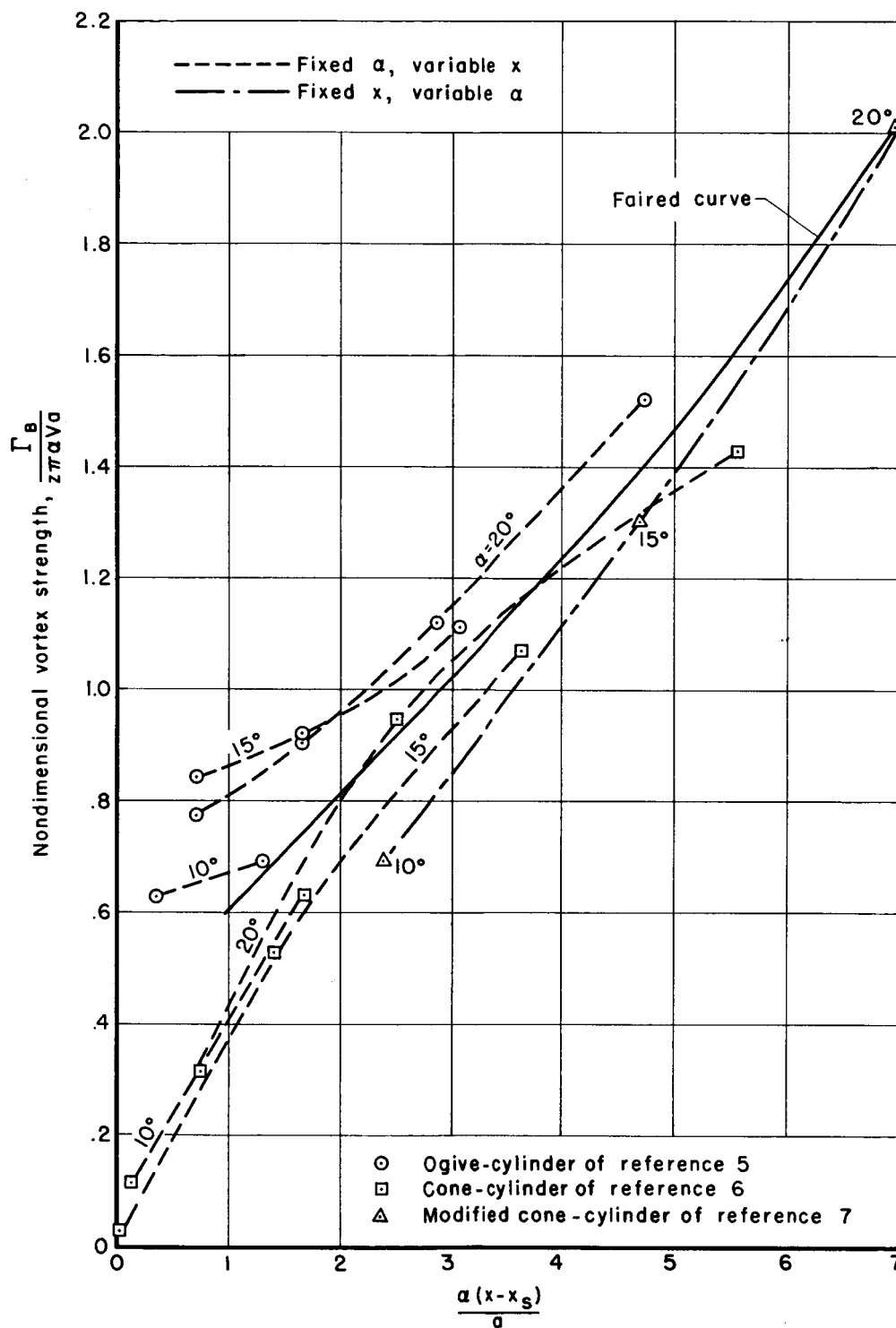
Figure 4.- Correlation of nondimensional vortex strengths for three bodies of revolution.
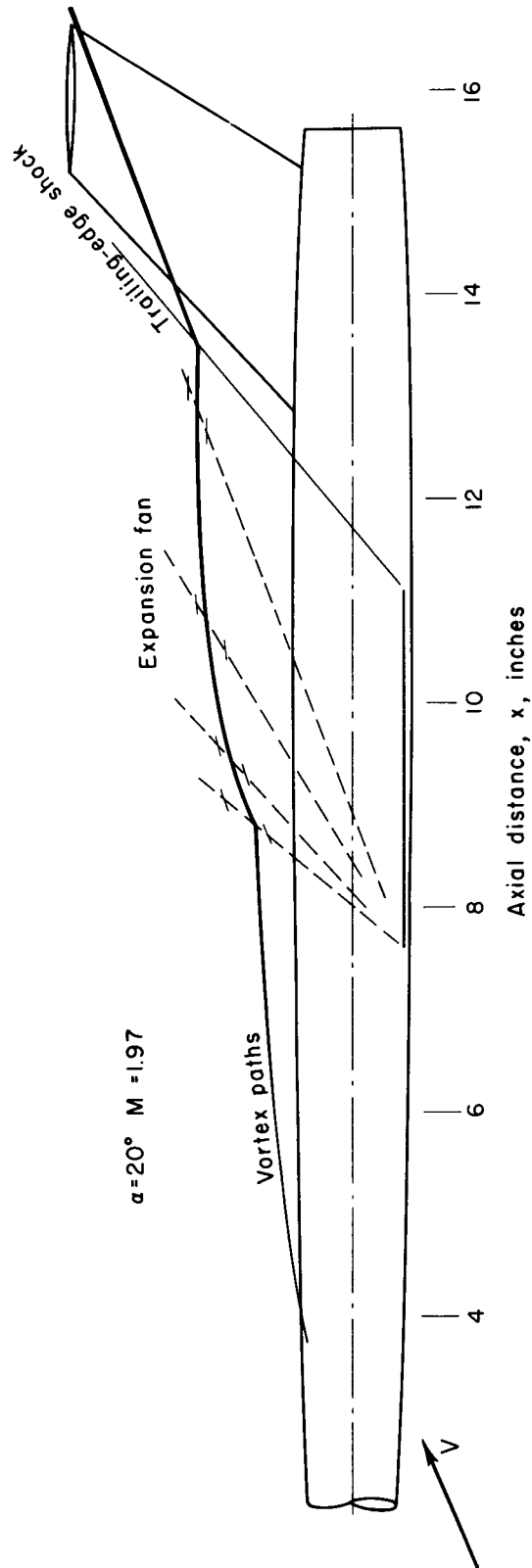
Figure 5.- Paths of body vortices for calculative example including influence of wing shock-expansion field.

CONFIDENTIAL

(a) $\alpha_W = 5^0$, M = 2.0
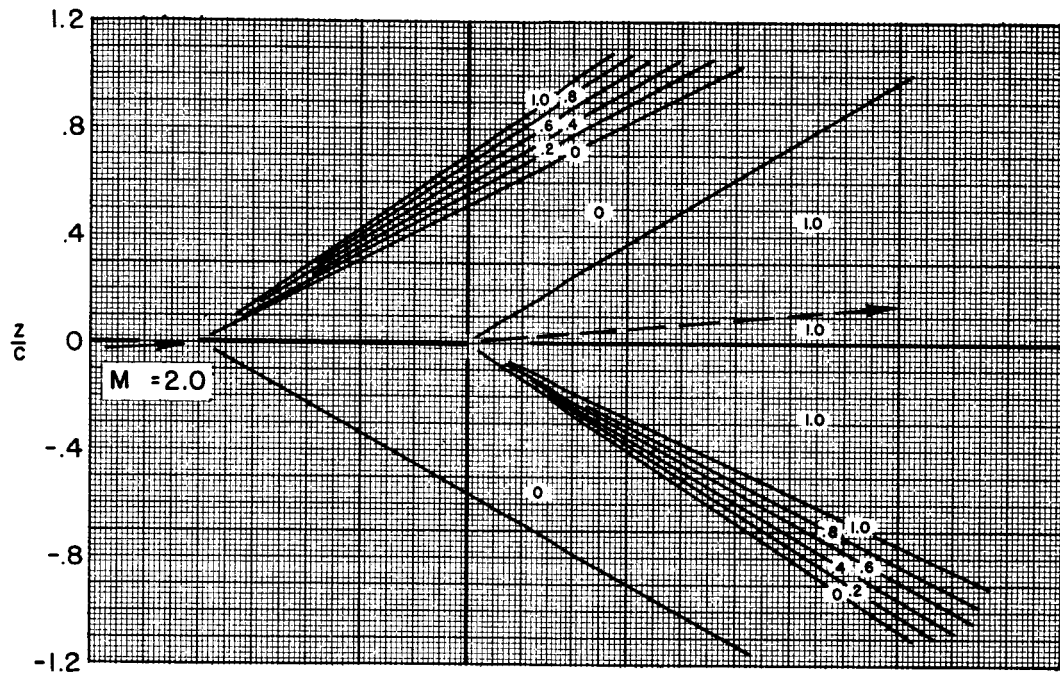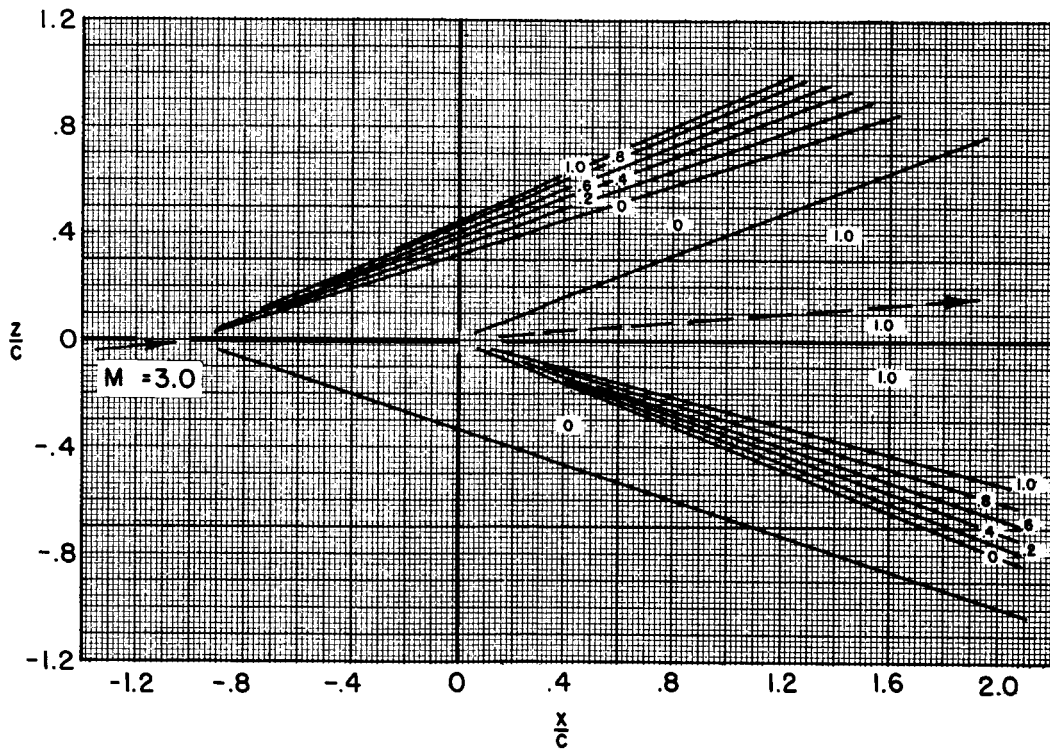
(b) $\alpha_W = 5^0$, M = 3.0

Figure 6.- Charts of tail effectiveness parameter η_α.
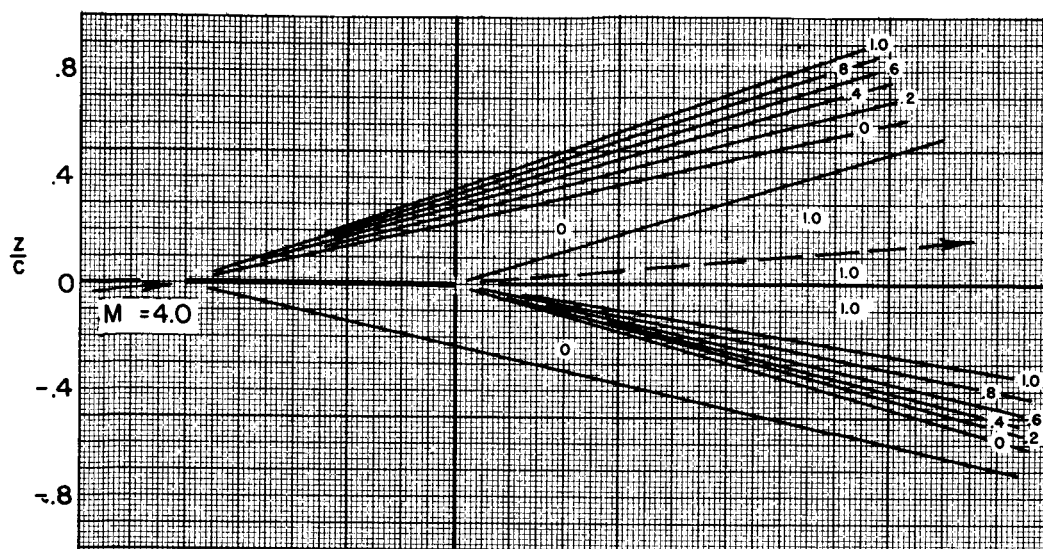
(c) $\alpha_w = 5^\circ$, $M = 4.0$
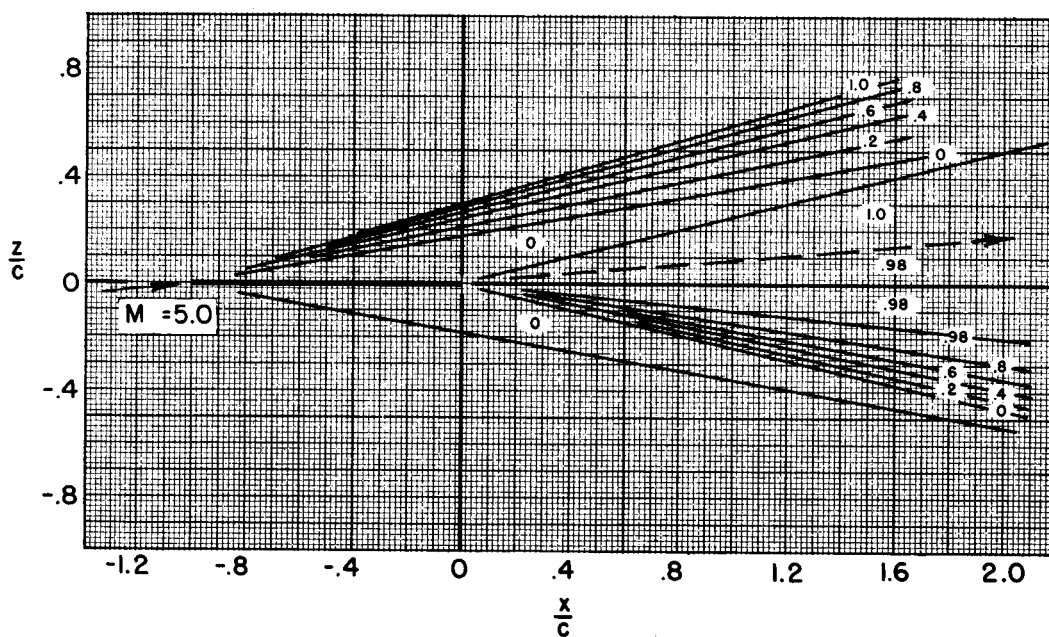
(d) $\alpha_w = 5^\circ$, $M = 5.0$

Figure 6.- Continued.
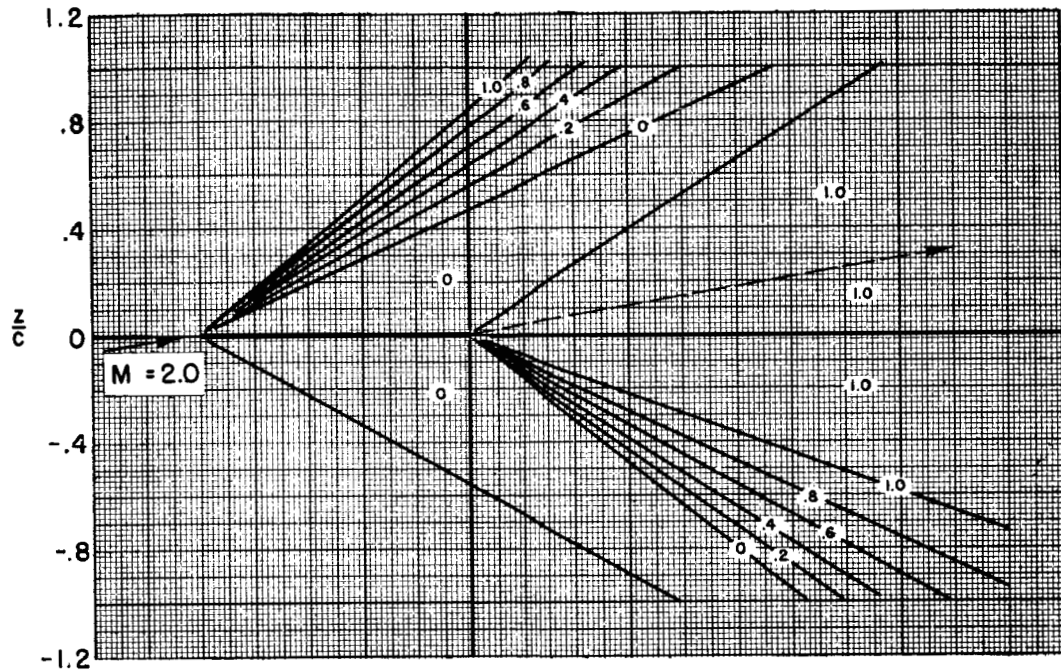
(e) $\alpha_w = 10^\circ$, $M = 2.0$
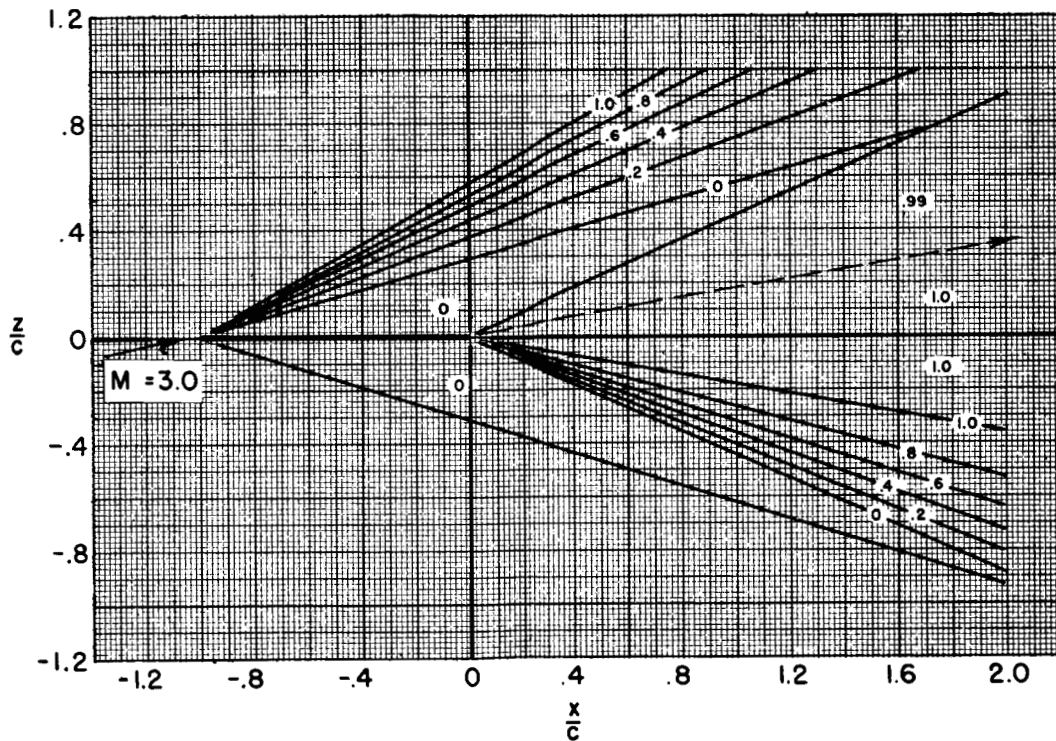
(f) $\alpha_w = 10^\circ$, $M = 3.0$

Figure 6.- Continued.
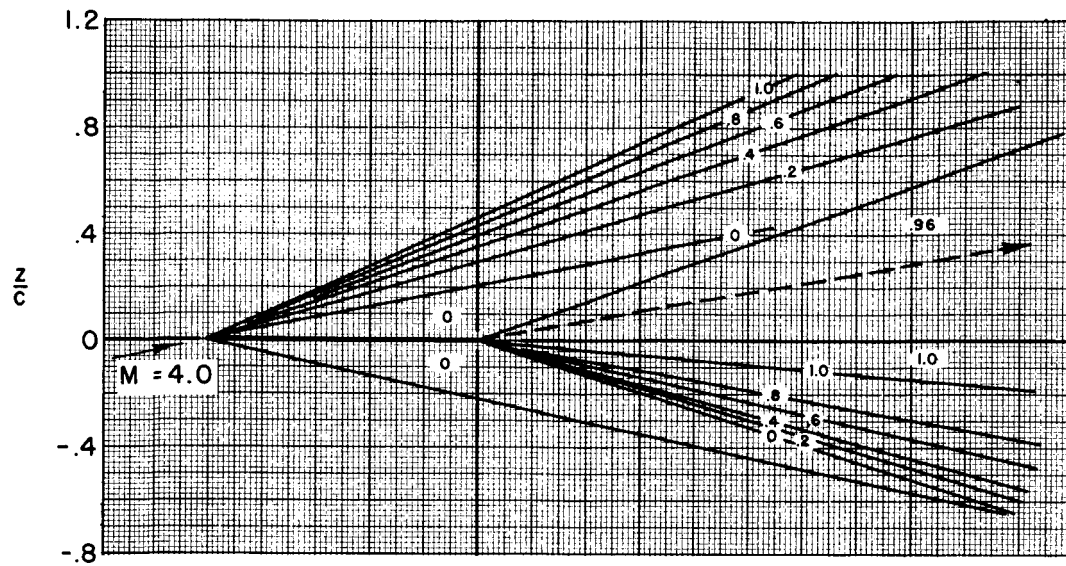
(g) $\alpha_w = 10°$, $M = 4.0$
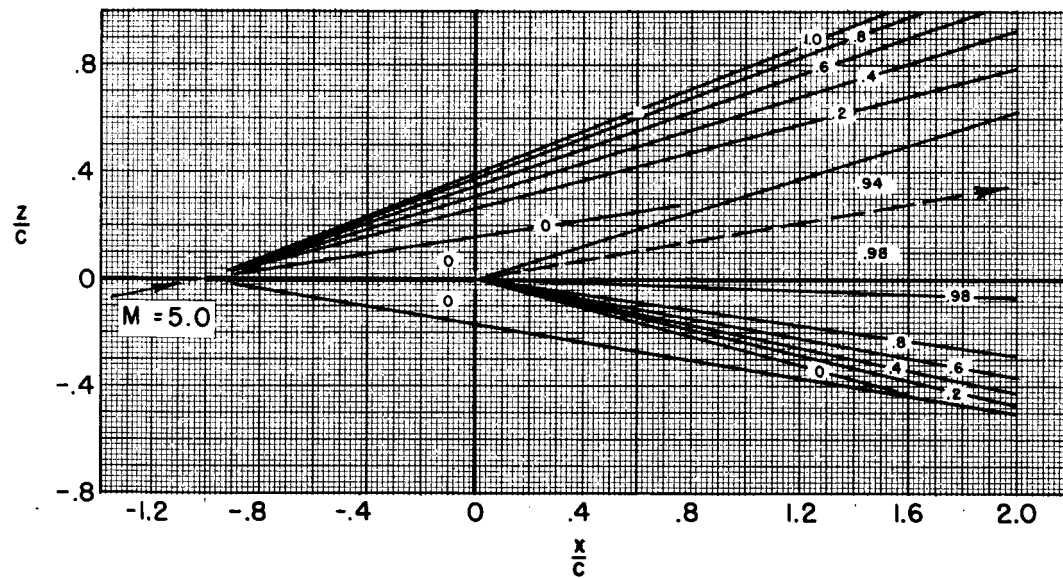
(h) $\alpha_w = 10°$, $M = 5.0$

Figure 6.- Continued.
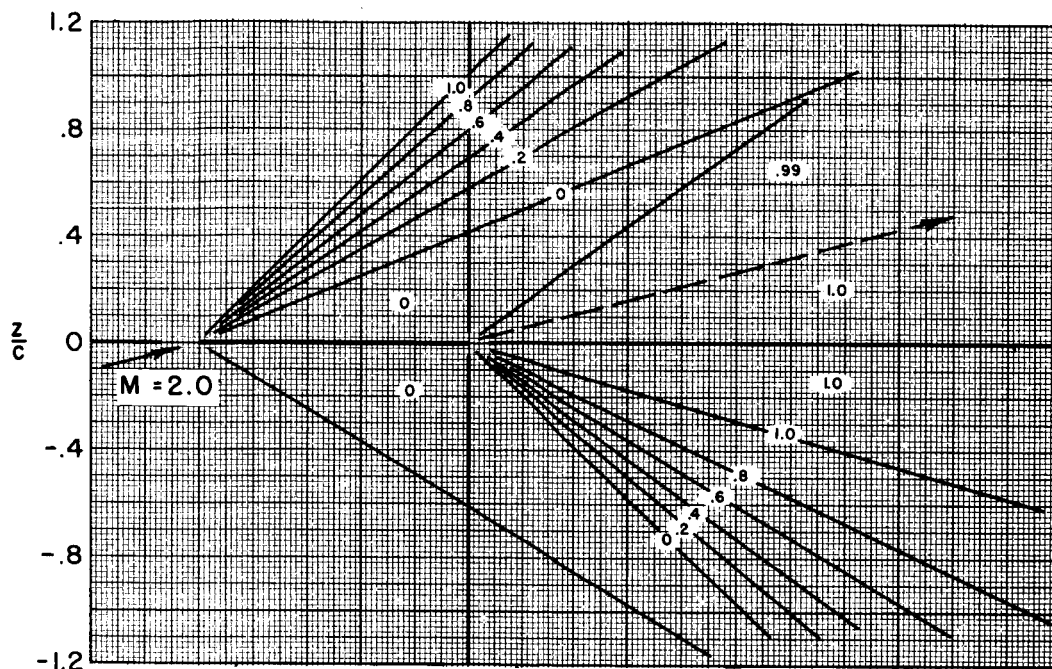
(i) $\alpha_w = 15°$, $M = 2.0$
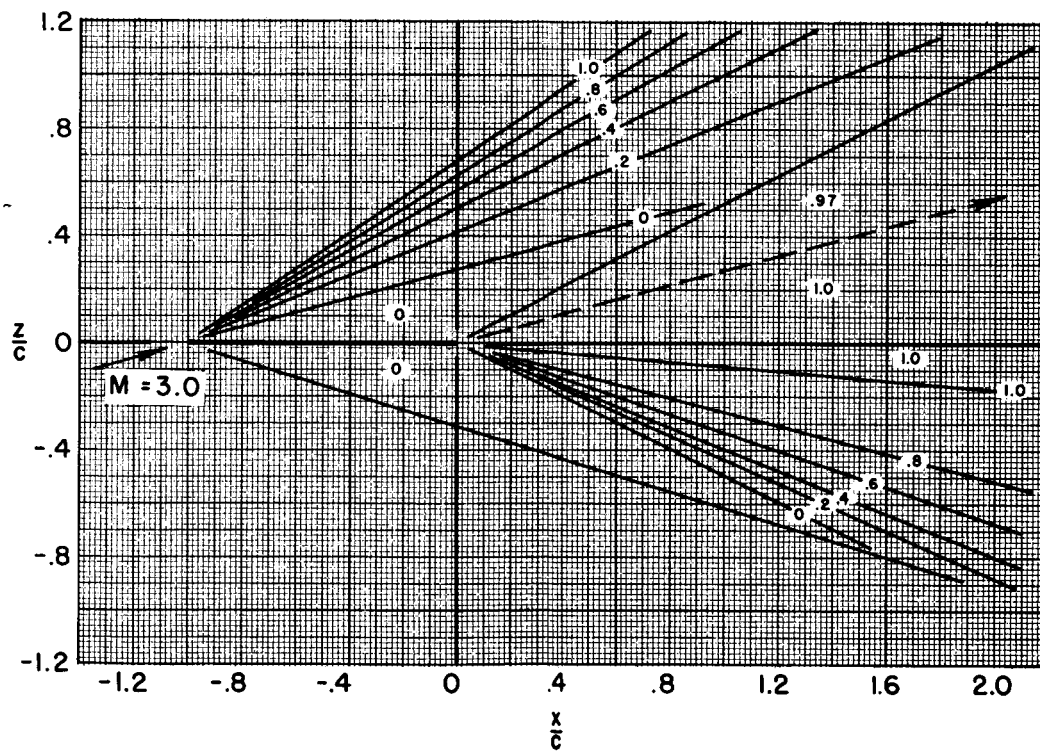
(j) $\alpha_w = 15°$, $M = 3.0$

Figure 6.- Continued.
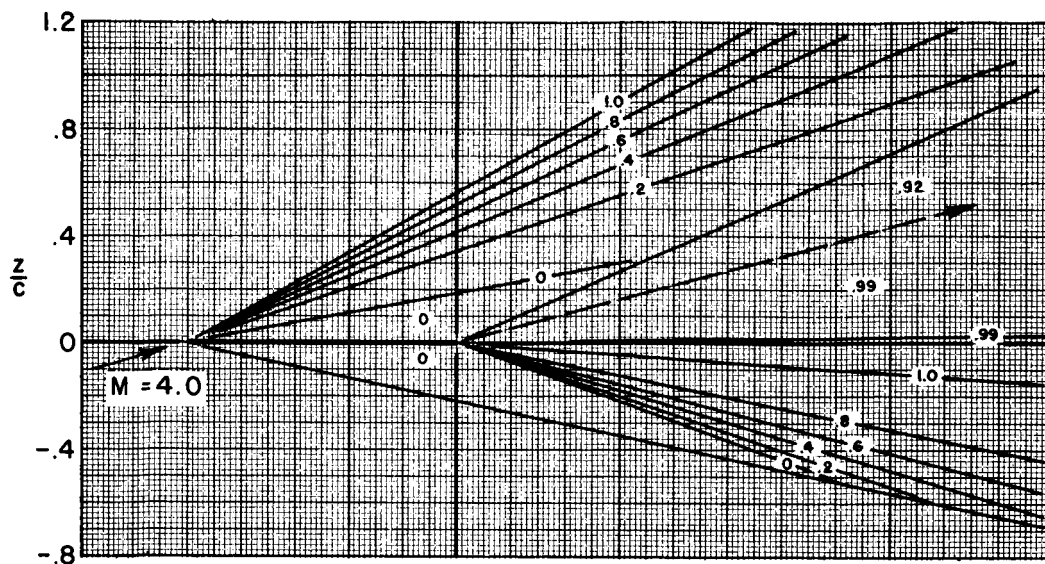
(k) $\alpha_w = 15^\circ$, M = 4.0
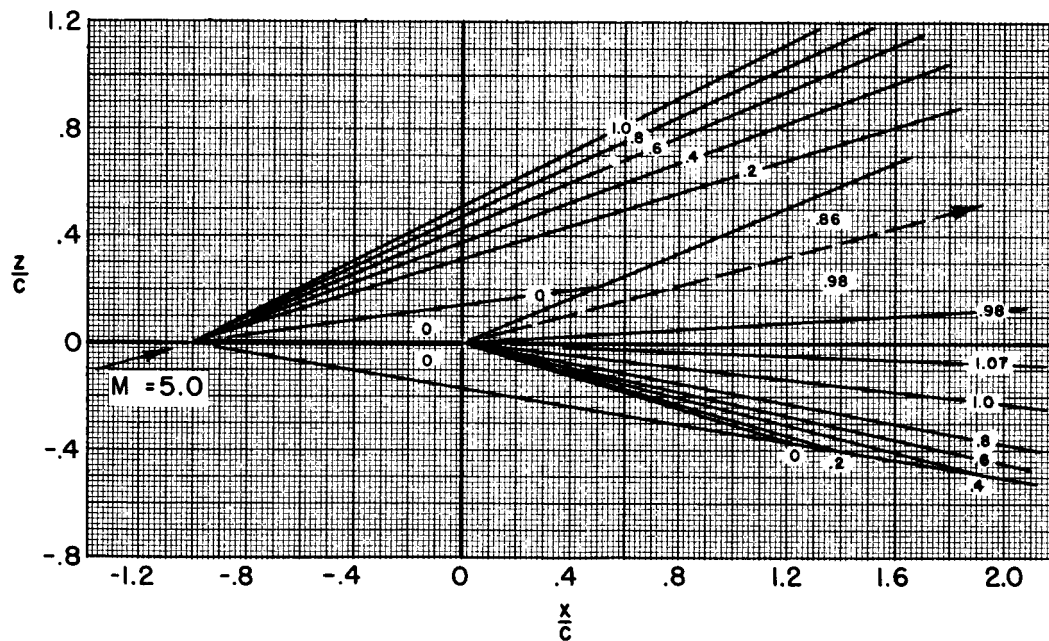
(l) $\alpha_w = 15^\circ$, M = 5.0

Figure 6.- Continued.

(m) $\alpha_W = 20^O$, M = 2.0

(n) $\alpha_W = 20^O$, M = 3.0
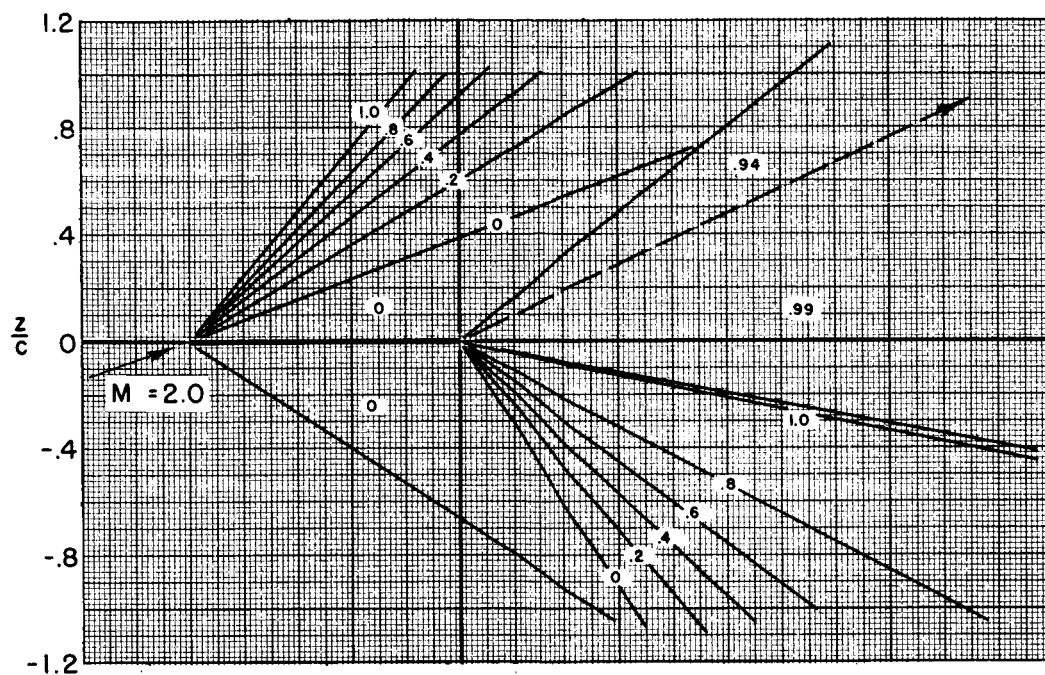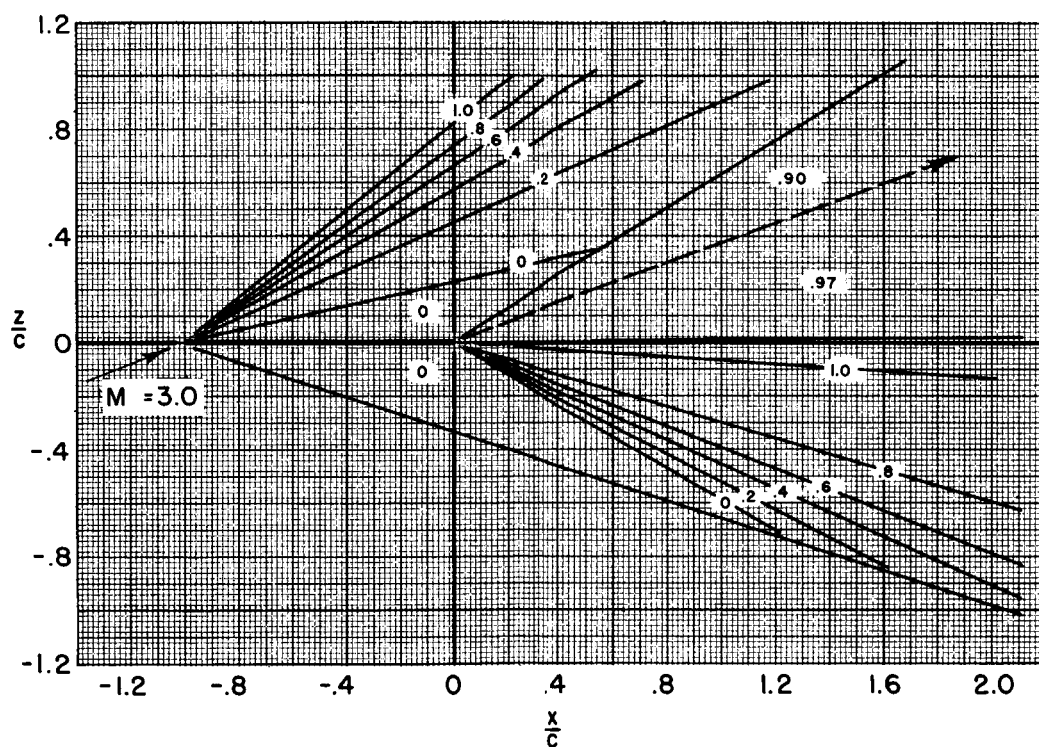
Figure 6.- Continued.
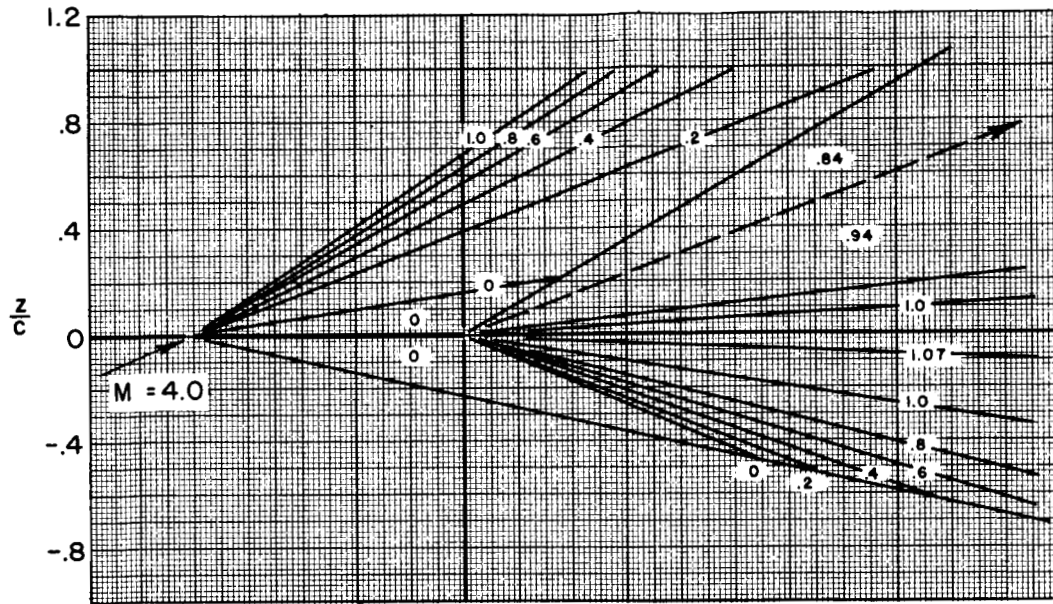
(o) $\alpha_w = 20°$, M = 4.0
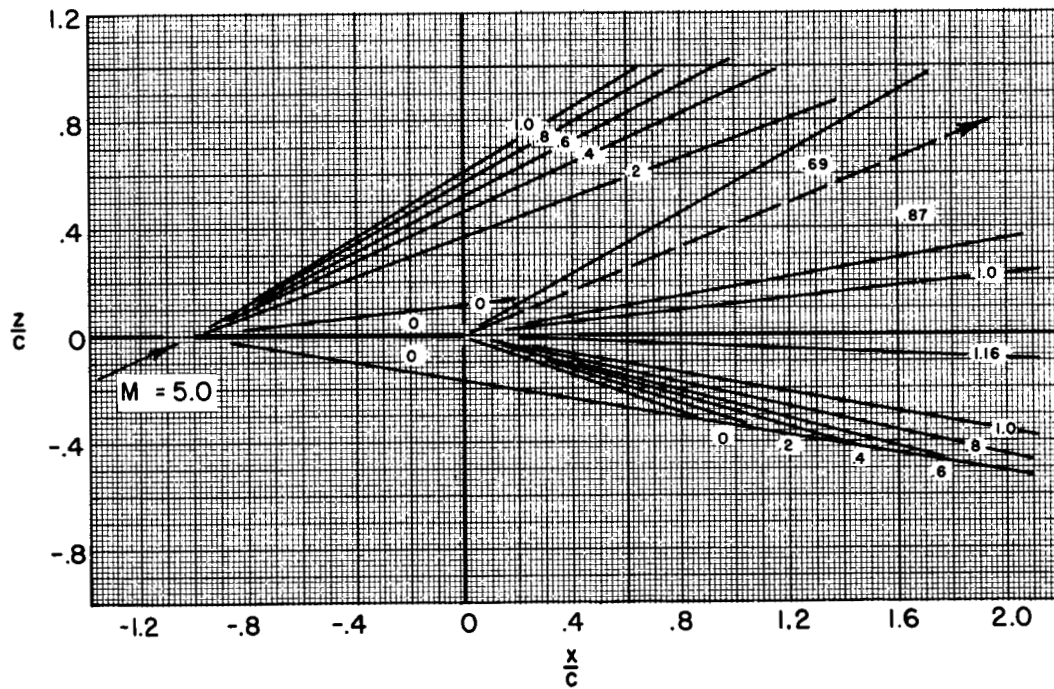
(p) $\alpha_w = 20°$, M = 5.0

Figure 6.- Concluded.
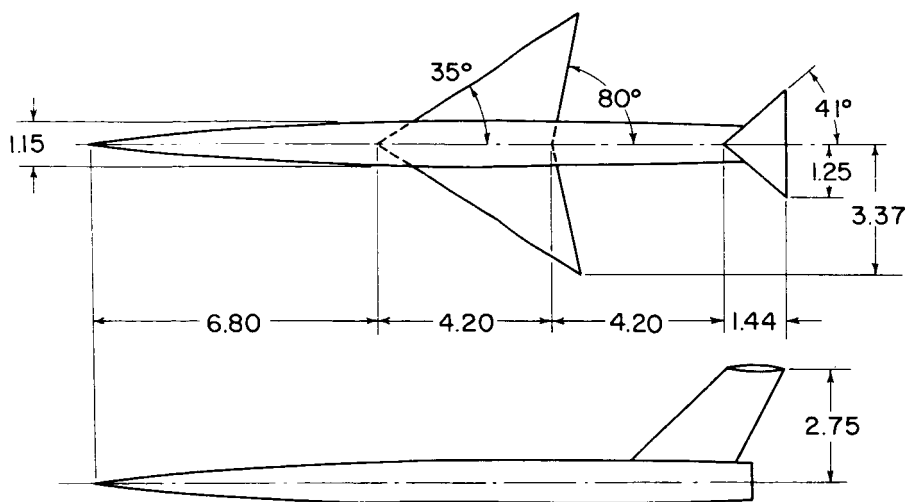
(a) Arrow-wing interceptor.
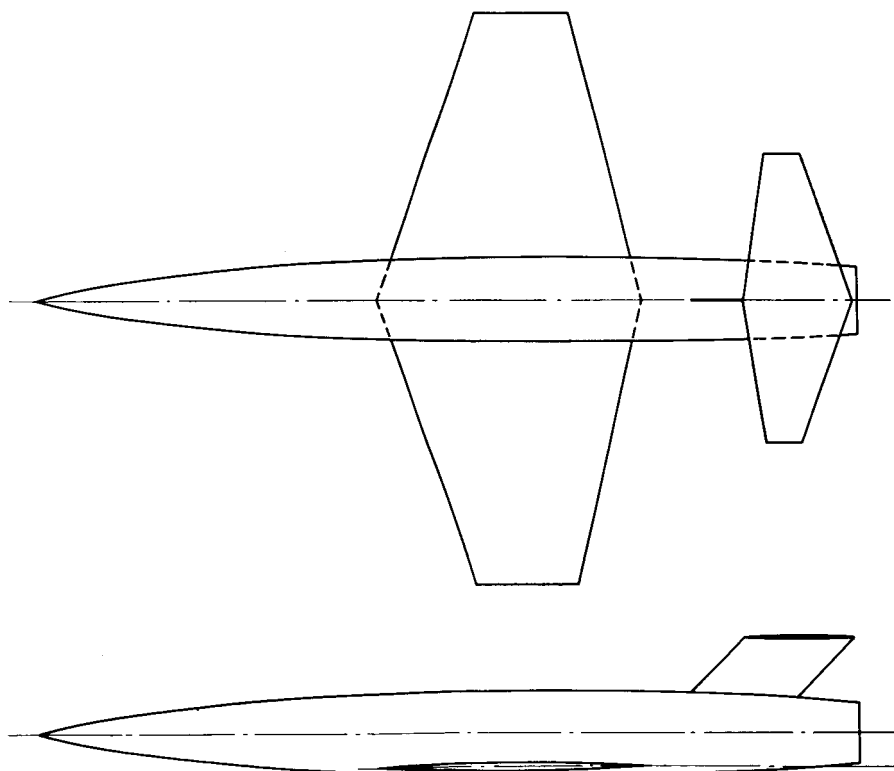
(b) Research model.

Figure 7.- Airplanes for which calculated pitch-up characteristics are compared with the measured characteristics.
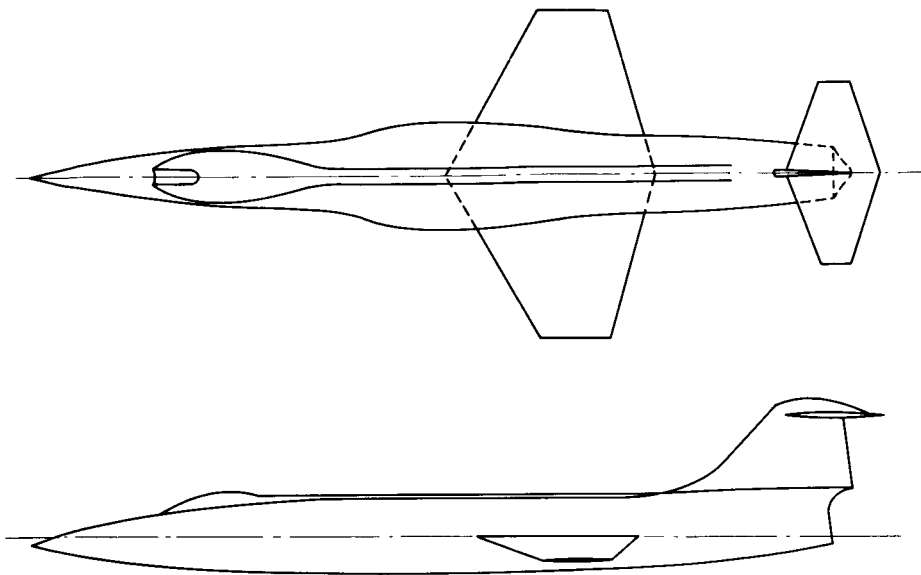
(c) Straight-wing airplane.
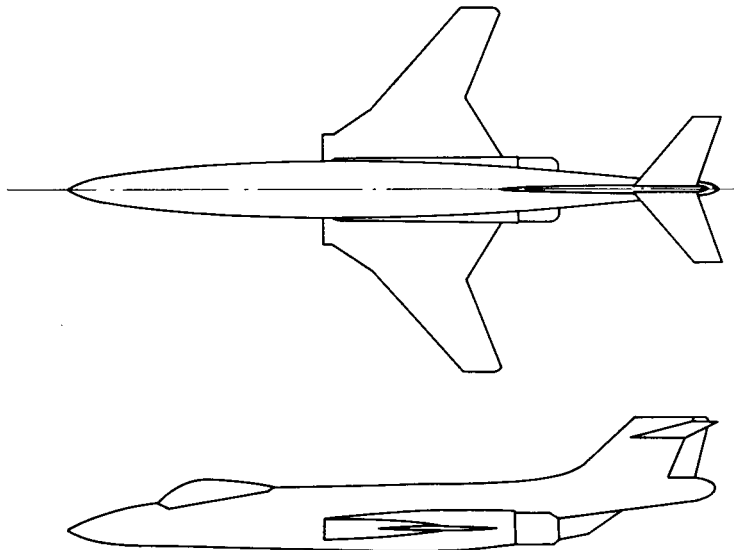
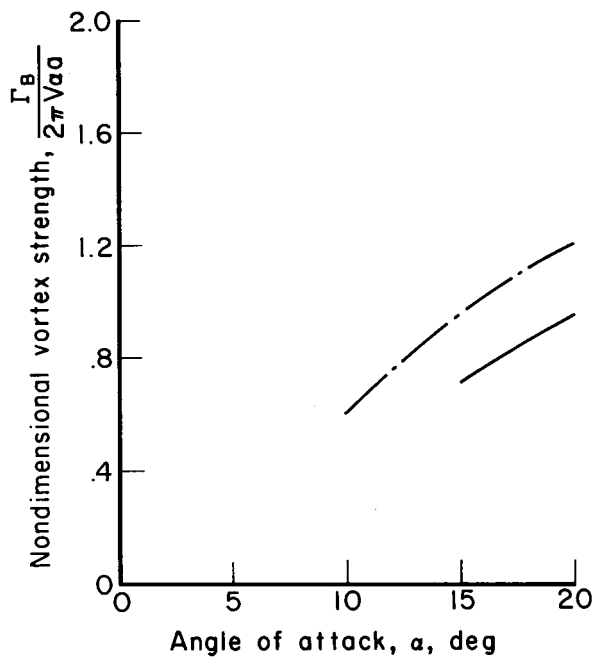(d) Swept-wing airplane.

Figure 7.- Concluded.
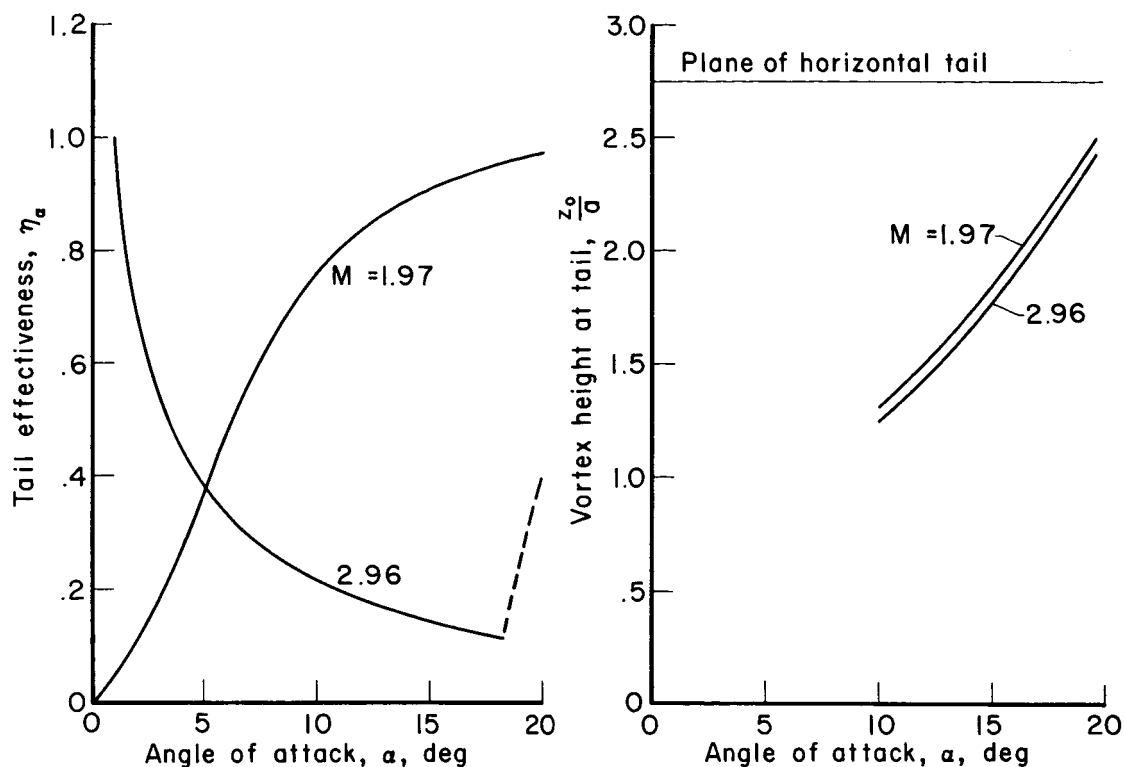
(a) Tail effectiveness parameter.

(b) Vortex height at tail.
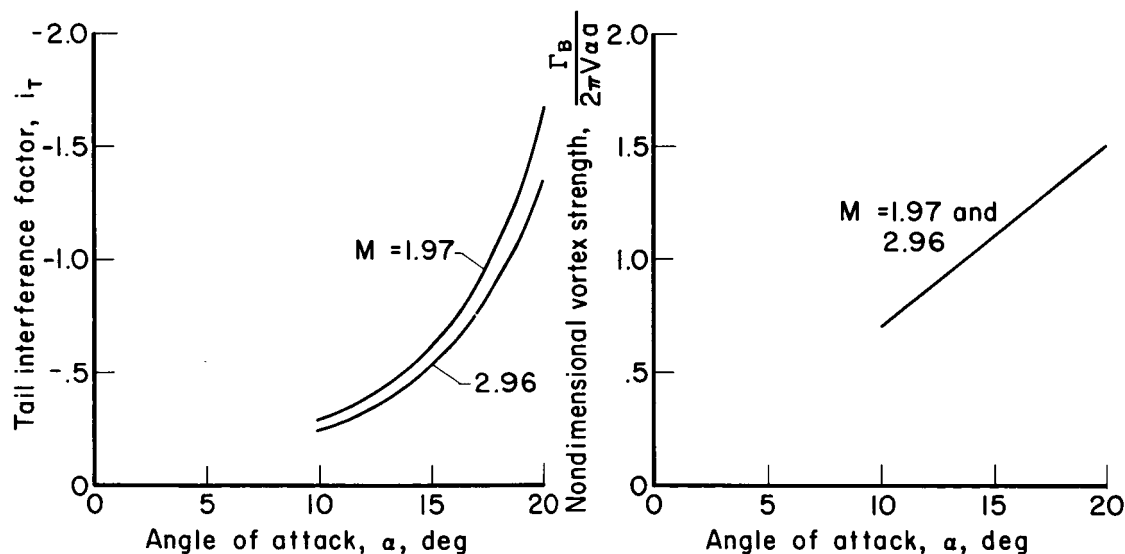
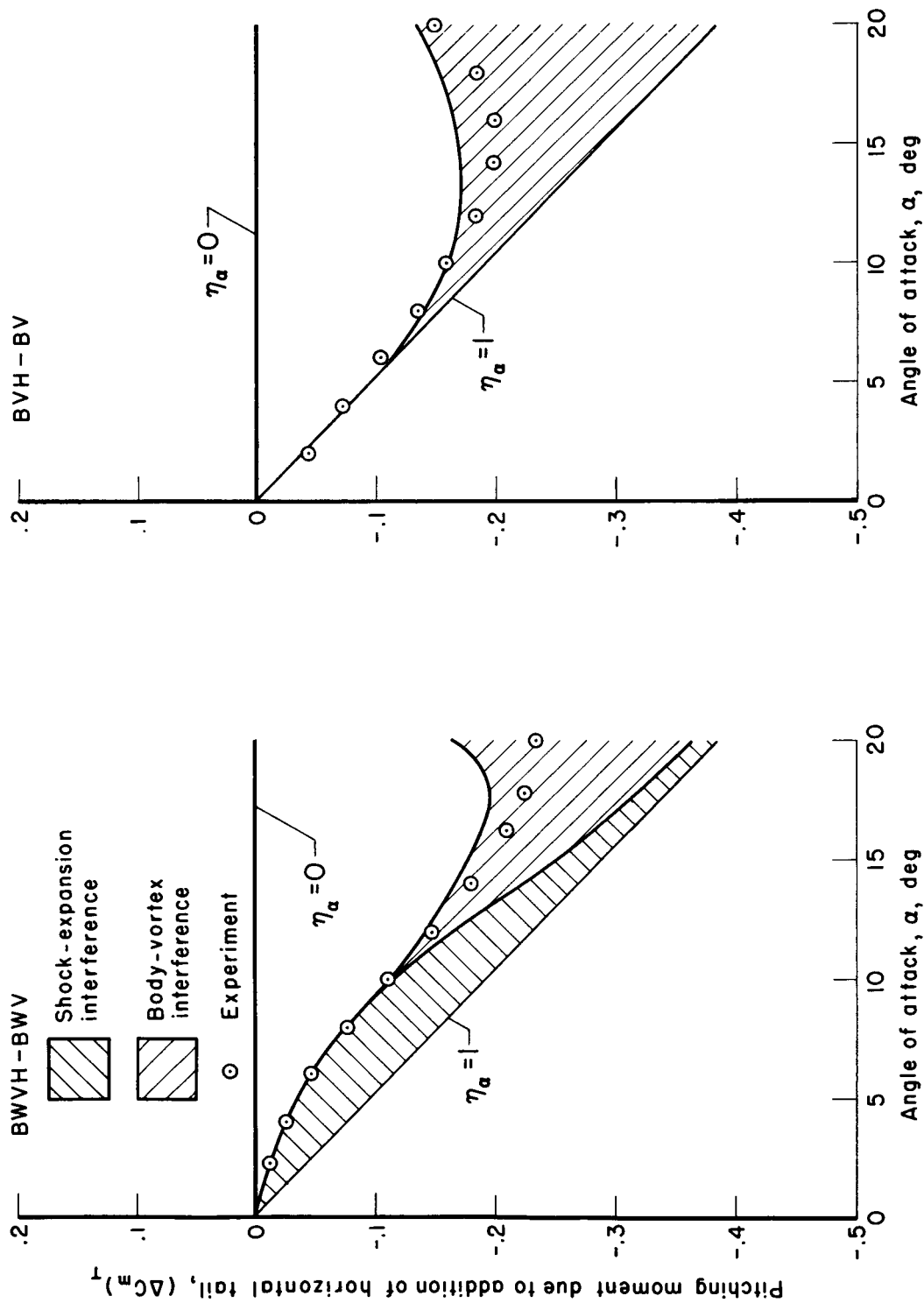(c) Tail interference factor.

(d) Nondimensional vortex strength.

Figure 8.- Variation with angle of attack for various parameters of arrow-wing-interceptor.
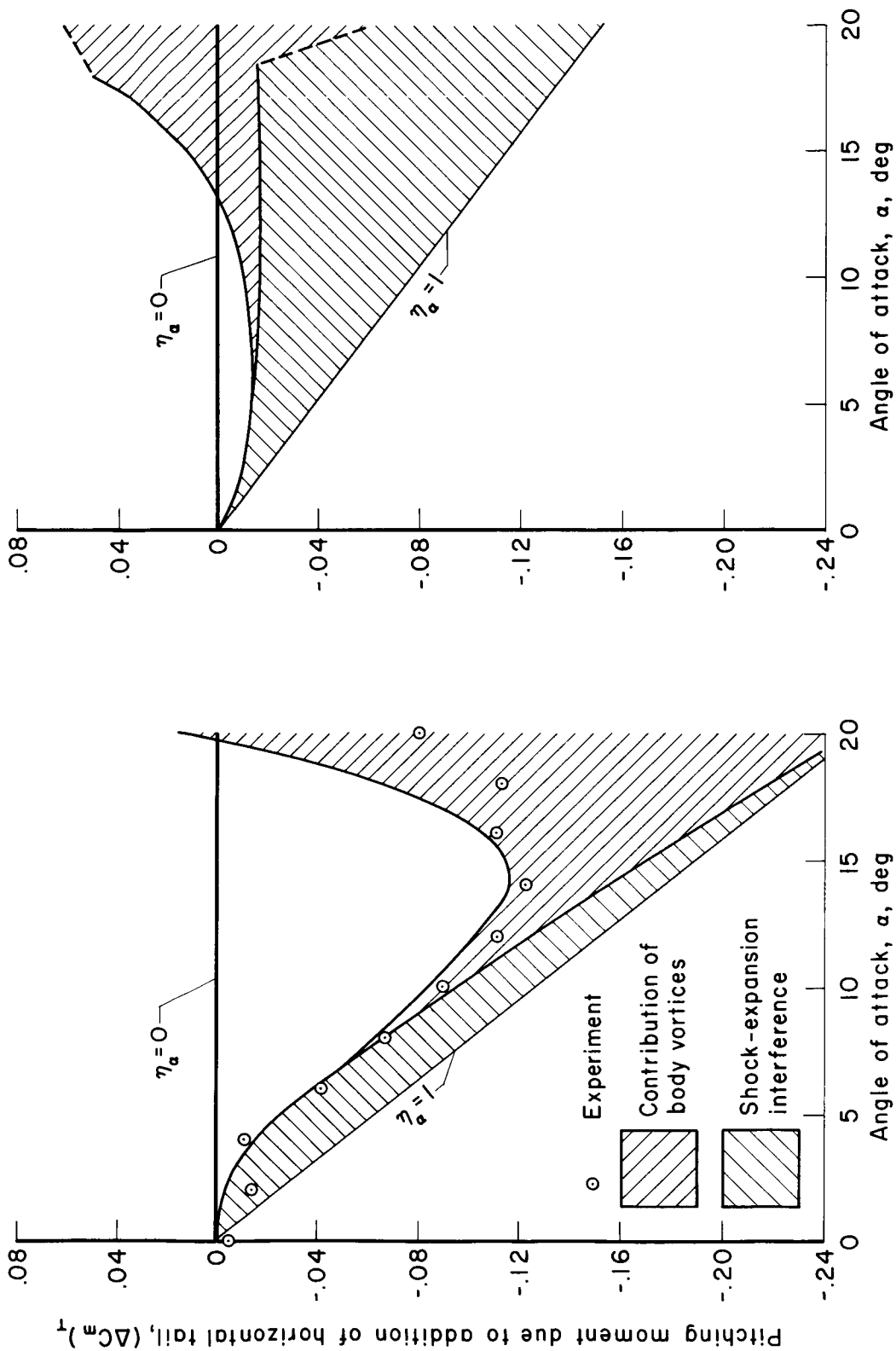
Figure 9.- Contribution of horizontal tail to pitching moment for arrow-wing interceptor.
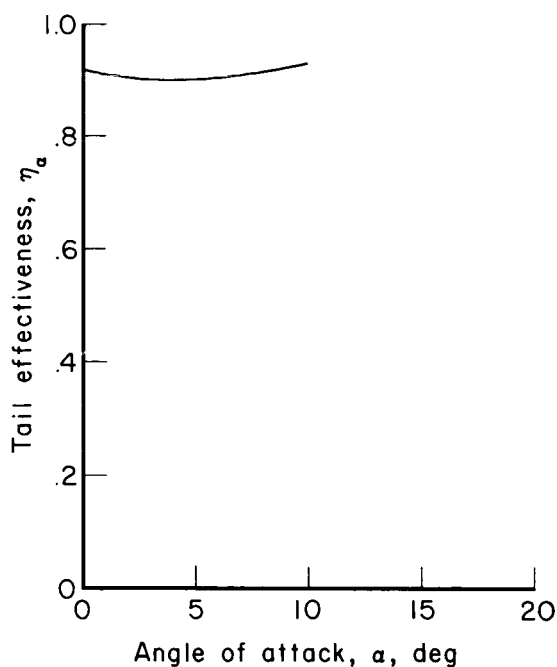
(a) Tail effectiveness parameter.
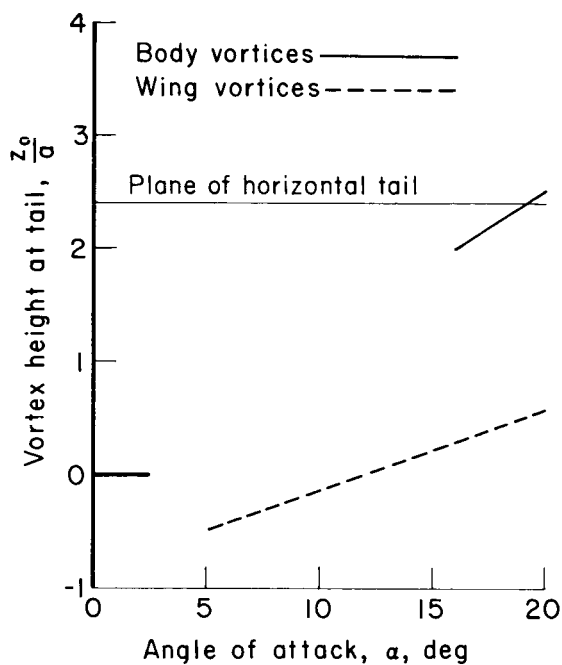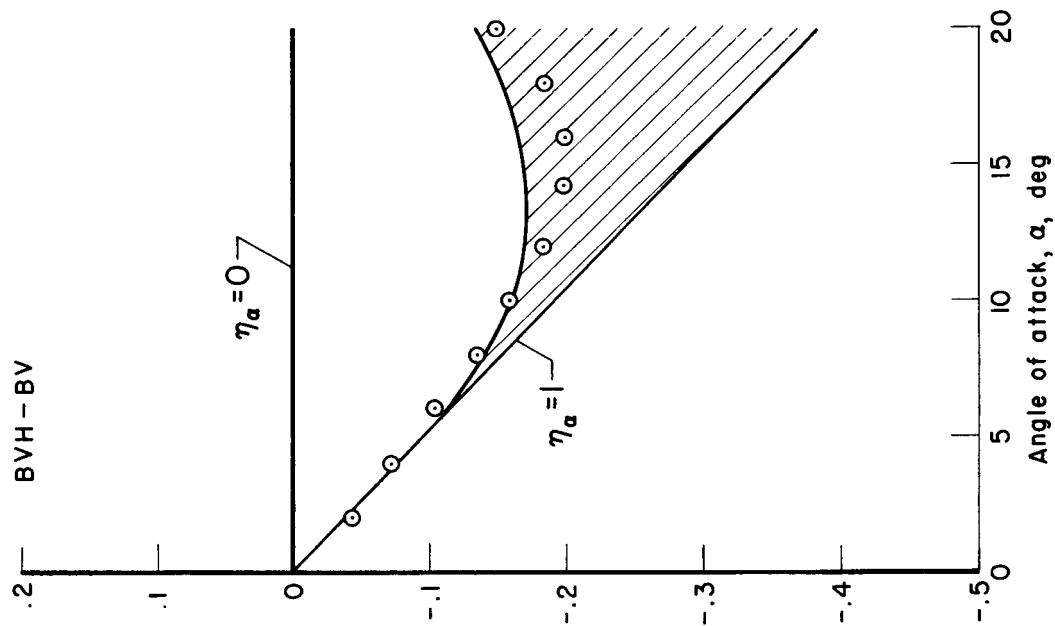
(b) Vortex height at tail.
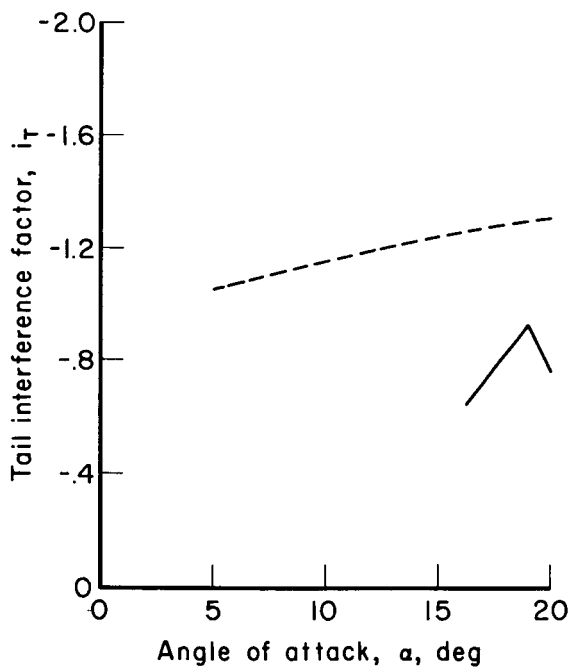
(c) Tail interference factor.
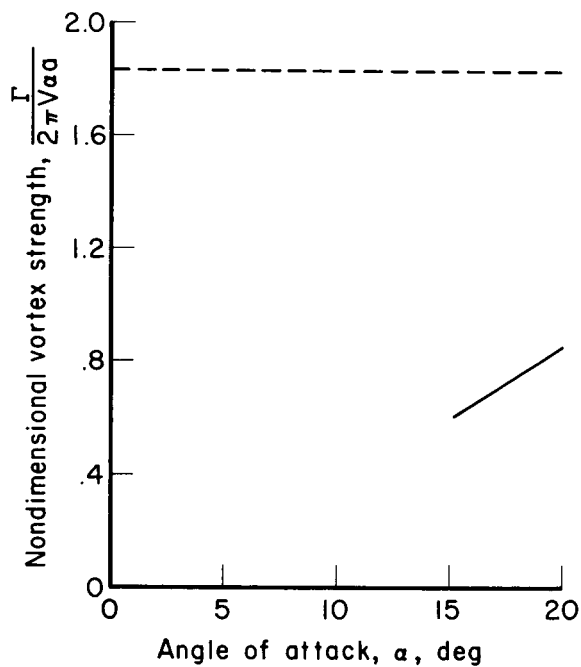
(d) Nondimensional vortex strength.

Figure 10.- Variation with angle of attack for various parameters for research model; M = 1.4.
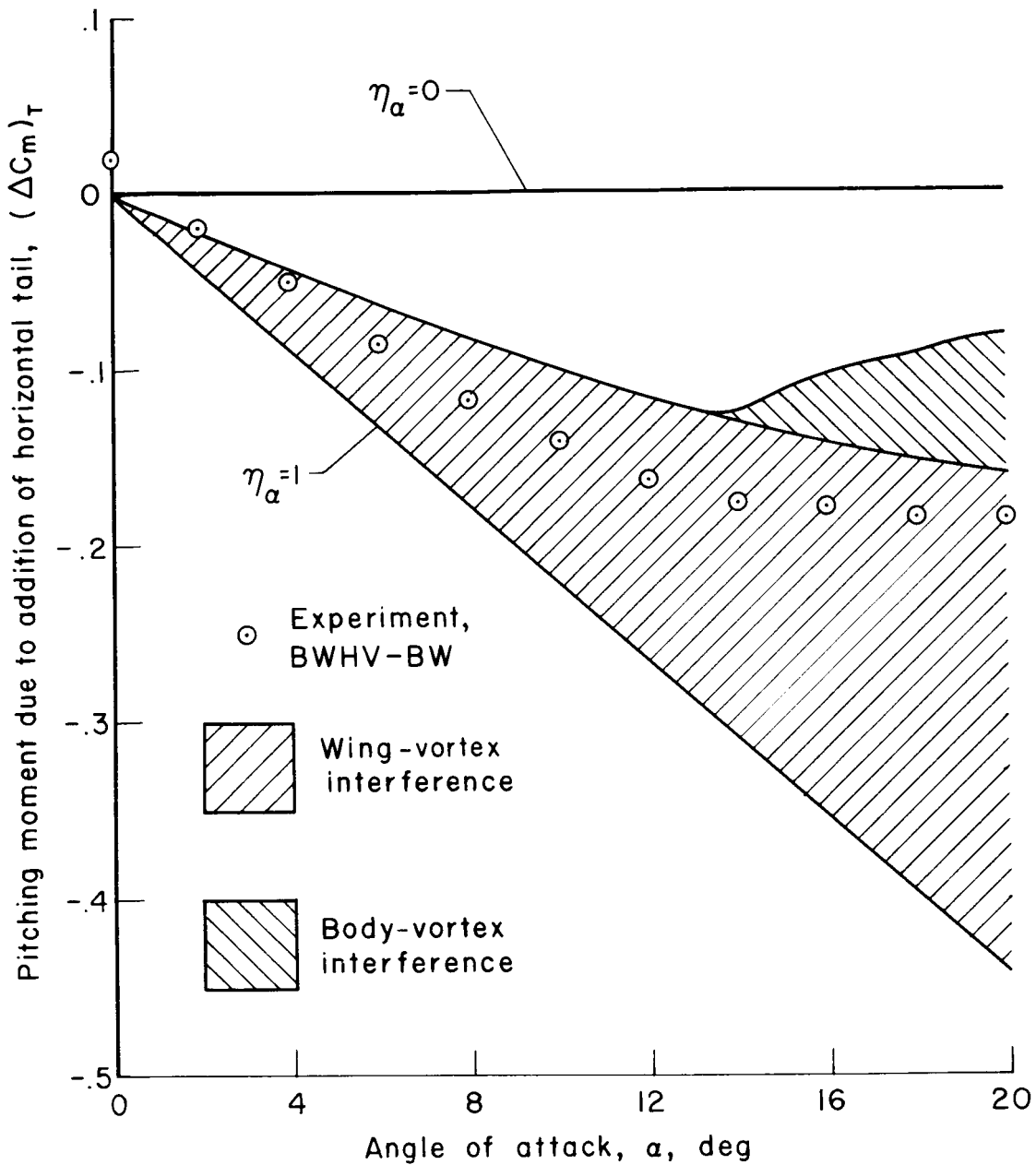
Figure 11.- Contribution of horizontal tail to pitching moment of research model; M = 1.4.
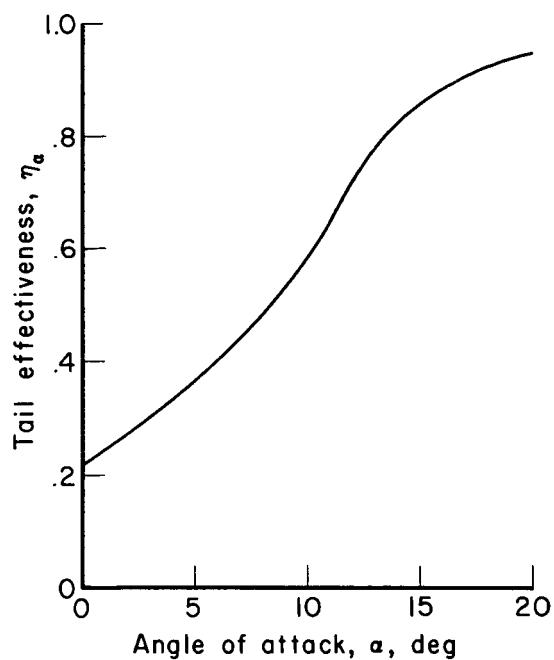
(a) Tail effectiveness parameter
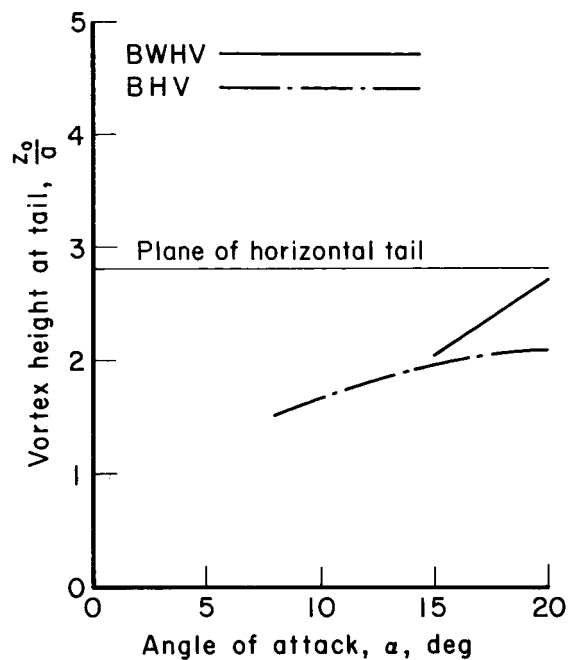
(b) Vortex height at tail.
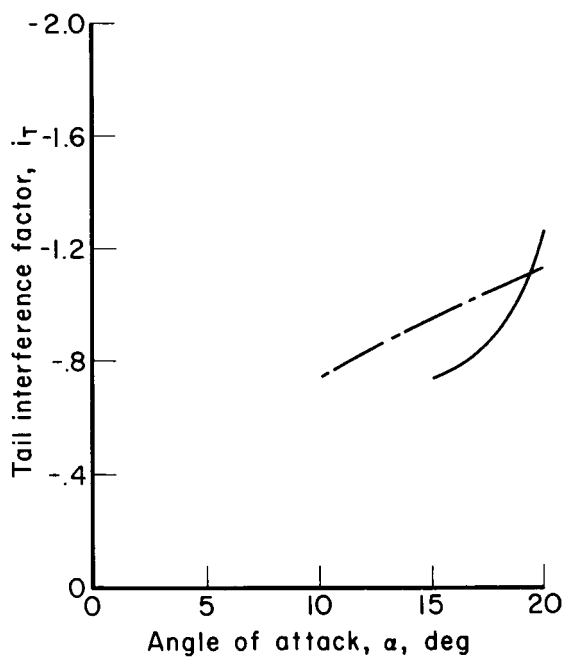
(c) Tail interference factor.

(d) Nondimensional vortex strength.

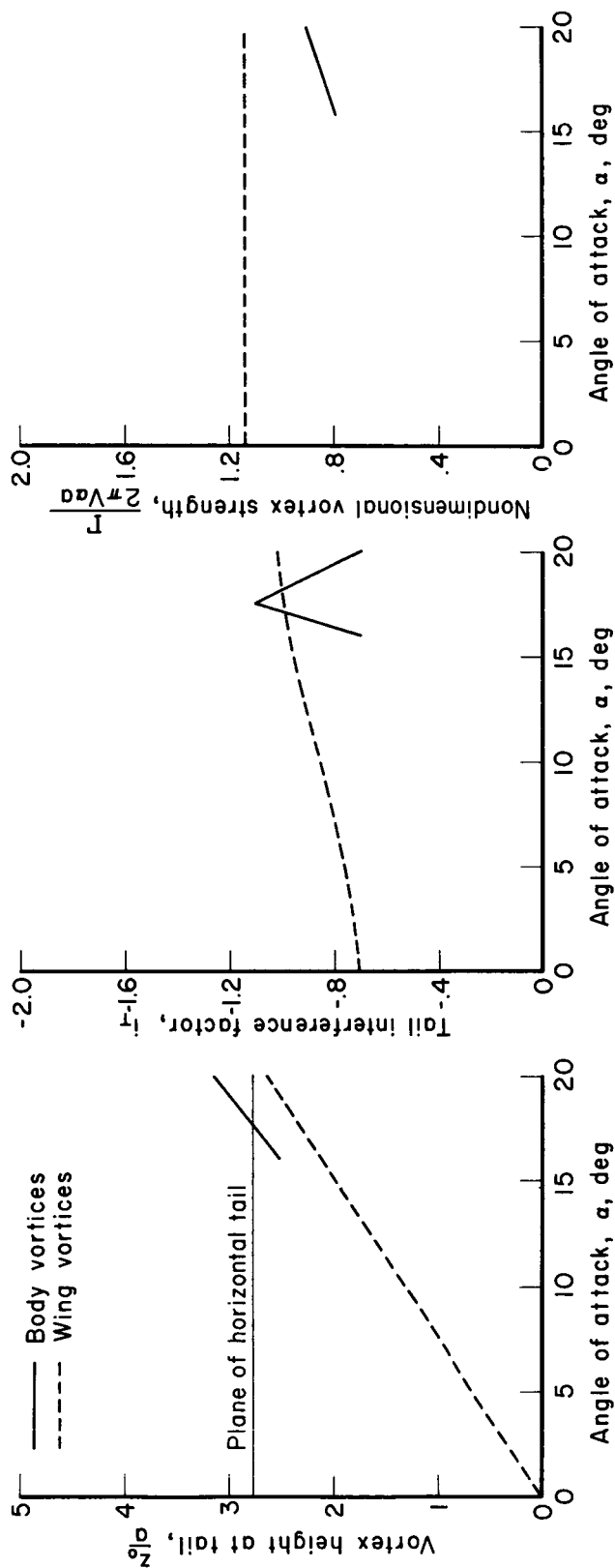Figure 12.- Variation with angle of attack of various parameters for straight-wing airplane; M = 2.01.

Figure 13.- Contribution of horizontal tail to pitching moment of straight-wing airplane; M = 2.01.

(a) Body-wing-tail combination.

(b) Body-tail combination.

(a) Vortex height at tail.   (b) Tail interference factor.   (c) Nondimensional vortex strength.

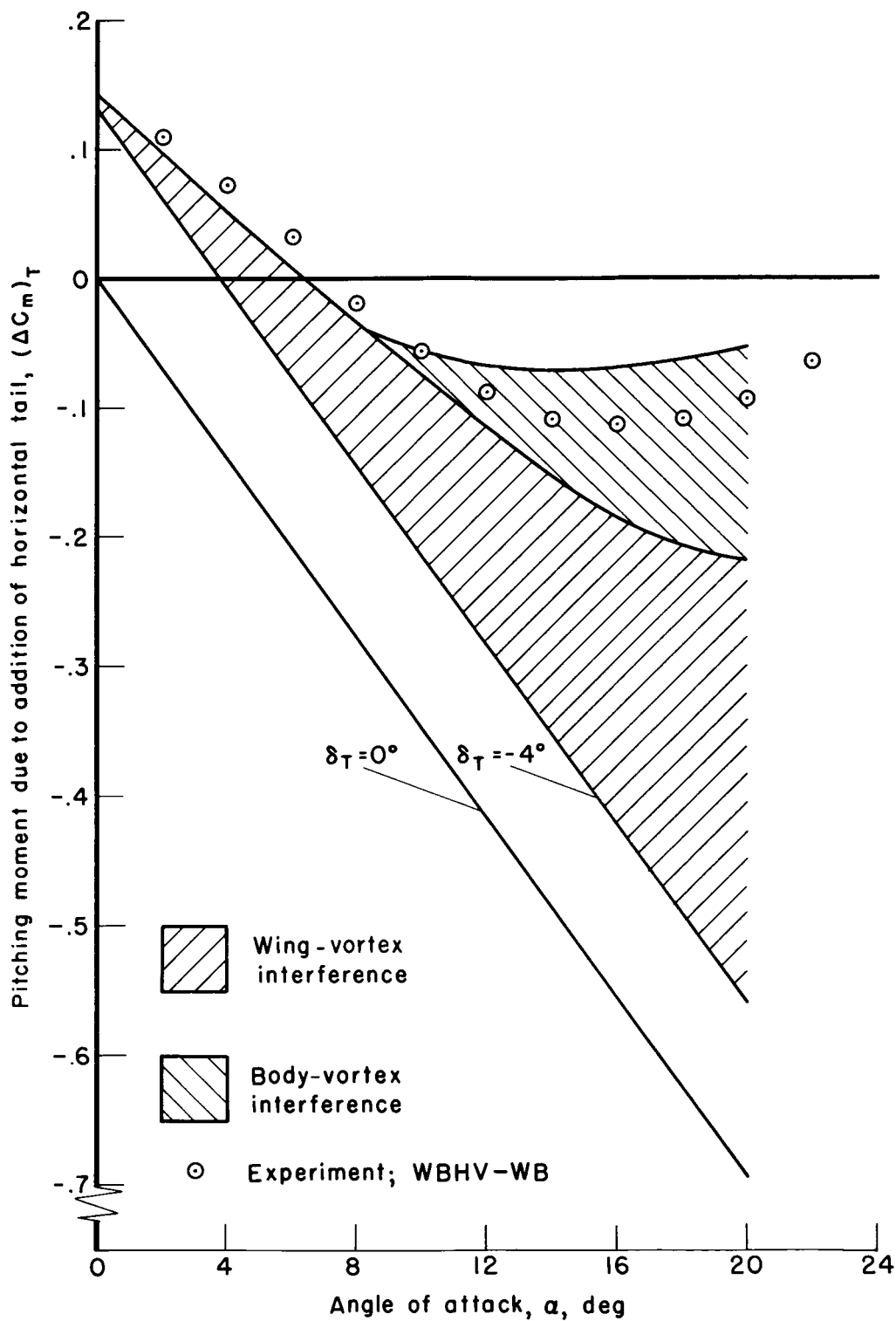Figure 14.- Variation with angle of attack of various parameters for swept-wing airplane; M = 1.56.

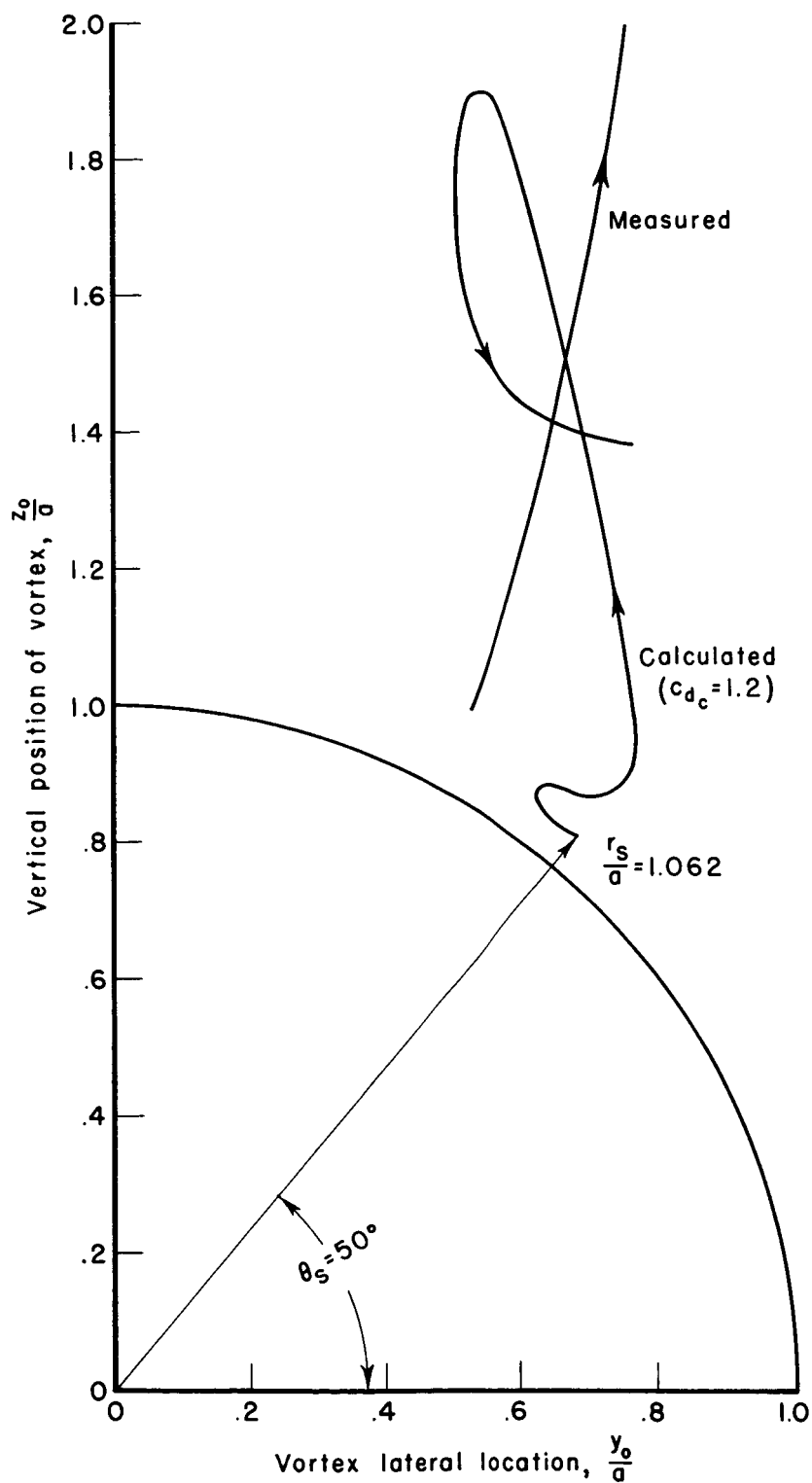Figure 15.- Contribution of horizontal tail to pitching moment of swept-wing airplane; M = 1.56.

Figure 16.- Comparison of calculated and measured vortex paths.